catalysts

MDPI

Article

Facile Synthesis of Sodium Alginate (SA)-Based Quaternary Bio-Nanocomposite (SA@Co-Zn-Ce) for Antioxidant Activity and Photocatalytic Degradation of Reactive Red 24

Sidra Fatima [1], Sana Javaid [2], Hira Ahmad [3], Afaf Almasoudi [4], Doaa F. Baamer [4], Omar Makram Ali [5], Sónia A. C. Carabineiro [6,*] and Muhammad Babar Taj [1,*]

[1] Institute of Chemistry, The Islamia University of Bahawalpur, Bahawalpur 63100, Pakistan; sidrafatima867@gmail.com

[2] Institute of Physics, The Islamia University of Bahawalpur, Bahawalpur 63100, Pakistan; sanajavaid764@gmail.com

[3] Department of Forensic Chemistry, Government College University, Lahore 54000, Pakistan; hirach160@gmail.com

[4] Chemistry Department, Faculty of Science, King Abdulaziz University, Jeddah P.O. Box 42734, Saudi Arabia; asalmasoudi@kau.edu.sa (A.A.); dfbaamer@kau.edu.sa (D.F.B.)

[5] Department of Chemistry, Taraba University College, Taraba Branch, Taif University, P.O. Box 11099, Taif 21944, Saudi Arabia; om.ali@tu.edu.sa

[6] LAQV-REQUIMTE, Department of Chemistry, NOVA School of Science and Technology, Universidade NOVA de Lisboa, 2829-516 Caparica, Portugal

* Correspondence: authors: sonia.carabineiro@fct.unl.pt (S.A.C.C.); dr.taj@iub.edu.pk (M.B.T.)

Abstract: This study introduces a new strategy for the environmentally friendly catalytic degradation of Reactive Red 24 (RR24) dye using sunlight. We developed a cost-effective quaternary nanocomposite by immobilizing a sodium alginate biopolymer over bioengineered Co-Zn-Ce nanoparticles, forming an SA@Co–Zn–Ce nanocomposite (where SA means sodium alginate). This composite also demonstrated an exceptional antioxidant potential of approximately 89%, attributed to the synergistic effect of sodium alginate and green-synthesized Co–Zn–Ce nanoparticles (biosynthesized using *Ocimum sanctum* leaf extract as a reducing agent). Scanning electron microscopy revealed grain sizes of 28.6 nm for Co–Zn–Ce NPs and 25.59 nm for SA@Co–Zn–Ce nanocomposites (NCs). X-ray diffraction showed particle sizes of 16.87 nm and 15.43 nm, respectively. Co–Zn–Ce NPs exhibited a zeta potential of 1.99 mV, whereas the sodium alginate-anchored Co–Zn–Ce showed −7.99 mV. This indicated the entrapment of negatively charged ions from sodium alginate, altering the surface charge characteristics and enhancing the photocatalytic degradation of RR24. Dynamic light scattering revealed an average particle size of approximately 81 nm for SA@Co–Zn–Ce NCs, with the larger size due to the influence of water molecules in the colloidal solution affecting hydrodynamic diameter measurement. The SA@Co–Zn–Ce NCs exhibited a CO_2 adsorption capacity of 3.29 mmol/g at 25 °C and 4.76 mmol/g at 40 °C, indicating temperature-dependent variations in adsorption capabilities. The specific surface area of Co–Zn–Ce oxide NPs, measured using Brunauer–Emmett–Teller (BET) analysis, was found to be 167.346 m^2/g, whereas the SA@Co–Zn–Ce oxide nanocomposite showed a surface area of 24.14 m^2/g. BJH analysis revealed average pore diameters of 34.60 Å for Co–Zn–Ce oxide NPs and 9.26 Å for SA@Co–Zn–Ce oxide NCs. Although the immobilization of sodium alginate on Co–Zn–Ce oxide NPs did not increase the adsorption sites and porosity of the composite, as evidenced by the N2 adsorption–desorption isotherms, the SA@Co–Zn–Ce oxide NCs still demonstrated a high photocatalytic degradation efficiency of RR24.

Keywords: sodium alginate; bio-nanocomposite; antioxidant; dye degradation; reactive red 24

check for updates

Citation: Fatima, S.; Javaid, S.; Ahmad, H.; Almasoudi, A.; Baamer, D.F.; Ali, O.M.; Carabineiro, S.A.C.; Taj, M.B. Facile Synthesis of Sodium Alginate (SA)-Based Quaternary Bio-Nanocomposite (SA@Co-Zn-Ce) for Antioxidant Activity and Photocatalytic Degradation of Reactive Red 24. *Catalysts* **2024**, *14*, 471. https://doi.org/10.3390/catal14080471

Academic Editor: Roberto Fiorenza

Received: 22 June 2024
Revised: 16 July 2024
Accepted: 22 July 2024
Published: 24 July 2024

Copyright: © 2024 by the authors. Licensee MDPI, Basel, Switzerland. This article is an open access article distributed under the terms and conditions of the Creative Commons Attribution (CC BY) license (https://creativecommons.org/licenses/by/4.0/).

1. Introduction

With the constant growth of industrialization and urbanization, environmental pollution has become an escalating global concern, needing proactive efforts to alleviate its detrimental impacts [1,2]. In particular, the textile industry is one of the major contributors to pollution, discharging large amounts of toxic dyes into water bodies [3]. Reactive azo dyes are a significant portion of these released dyes. These compounds contain one or more azo (–N=N–) groups and heterocyclic and aromatic rings, along with functional groups such as chloride and sulfonates [4]. The azo groups pose multiple hazards due to their limited biodegradability. Therefore, it is crucial to effectively remove these dyes before they are discharged into the environment [5,6]. In response to this imperative, nanotechnology holds promise, utilizing the exceptional properties of nanomaterials to address environmental challenges [7,8]. Various approaches have been employed to treat reactive azo dyes in wastewater, including adsorption, photocatalysis, oxidation, and coagulation [9]. Among those, adsorption stands out as a highly efficient methodology for eliminating dye effluents, offering numerous advantages such as a straightforward design, minimal generation of harmful byproducts, cost-effectiveness, and excellent performance [10].

Ocimum sanctum, commonly known as the Tulsi plant, exhibits unique properties and has been extensively recognized for its pharmaceutical and therapeutic benefits [11]. Previously, leaf extracts of Tulsi have been commonly employed for the production of monometallic nanoparticles such as cobalt, zinc, cerium, silver, gold, and platinum [12]. Green synthesis methodologies ensure environmental sustainability in the manufacturing process and emphasize the importance of designing materials that minimize waste production and energy consumption. This aligns with the principles of green chemistry and promotes the development of eco-friendly solutions for wastewater treatment. The chemical value of the synthesized nanocatalyst holds great promise for the industrial, nanotechnological, and engineering fields [13].

Metal-based nanocomposites have garnered significant attention due to their exceptional adsorption and photocatalytic capabilities. Cobalt, as a monometallic element, demonstrates outstanding adsorption affinity, making it an ideal candidate for capturing dyes from wastewater [14]. The incorporation of zinc as a bimetallic component synergistically enhances the adsorption capacity and stability of the nanocomposite, facilitating efficient dye removal and recyclability through simple regeneration processes [15]. Moreover, the unique photocatalytic properties of cerium allow for the catalysis of the degradation of adsorbed dyes under light irradiation, transforming pollutants into benign byproducts [16]. Therefore, the incorporation of cerium enables the creation of a nanocomposite, synthesized for the first time in this work using *Ocimum sanctum*.

Sodium alginate is a biocompatible and biodegradable polysaccharide well known for its excellent film-forming and metal-ion-binding properties [17]. Its use as a template for the controlled synthesis of metal-based nanocomposites enhances the structural reliability and stability of the resulting composite, ensuring its eco-friendly nature [18]. These functionalities give the nanocomposite multifunctional innovative possibilities for sustainable wastewater treatment in industries struggling with dye pollution [19]. Sodium alginate beads have previously been studied for the removal of dyes such as reactive red 195 [20] and Orange 16 [21].

In this context, to further enhance stability, the incorporation of sodium alginate over bioinspired cobalt–zinc–cerium nanoparticles using *Ocimum sanctum* represents a novel approach to environmental pollution control. The chemical significance of the synthesized sodium alginate (SA)-anchored nanocomposite, SA@Co–Zn–Ce, reverberates across various sectors, notably in the textile industry. By providing a highly efficient and cost-effective photocatalytic degradation process for Reactive Red 24 (RR24) dye, the SA@Co–Zn–Ce nanocomposite offers a pathway to enhance wastewater treatment in textile manufacturing units [22]. The potential economic and environmental benefits are significant, reducing the industry's ecological footprint while complying with stringent environmental regulations [23].

This study explores the unique application of Tulsi plant extract as a reducing agent in the synthesis of cobalt–zinc–cerium oxide NPs. To the best of our knowledge, the synthesis of such oxide NPs has not been previously reported in the literature using *Ocimum sanctum*, which has mainly focused on monometallic cobalt, zinc, and cerium oxide NPs, as well as zinc-doped cerium oxide NPs. This research aims to fill this knowledge gap and establish the feasibility of using Tulsi extract as a sustainable reducing agent for the synthesis of unique nanomaterials. These materials are further stabilized with the addition of sodium alginate to form a novel nanocomposite, SA@Co–Zn–Ce. The structural, morphological, and compositional attributes of SA@Co–Zn–Ce have been explored using several characterization techniques. The main objective of this research article is to assess the antioxidant potential and photocatalytic degradation efficiency of SA@Co–Zn–Ce nanocomposites towards RR24 dye.

2. Results and Analysis

2.1. UV-vis

The UV-vis results of *Ocimum sanctum* leaf extract reveal a maximum absorption peak at 284 nm (Figure S1), likely due to aromatic substances such as alkaloids and flavonoids [24]. The synthesis of Co NPs using this extract resulted in a shift in absorption to 314 nm, indicating an interaction between the phytoconstituents and Co^{2+} ions (Figure 1) [25]. The addition of Zn to obtain Co–Zn oxide nanoparticles shifted the peak to 328 nm [26]. Incorporating Ce to produce the Co–Zn–Ce oxide nanoparticles led to multiple absorption peaks at 303, 351, and 376 nm, indicating complex nanoparticle formation [27]. Sodium alginate anchoring to Co–Zn–Ce oxide nanoparticles exhibited maximum absorption at 284 nm and some smooth peaks within the visible spectrum, possibly due to the interaction between sodium alginate and the nanoparticles.

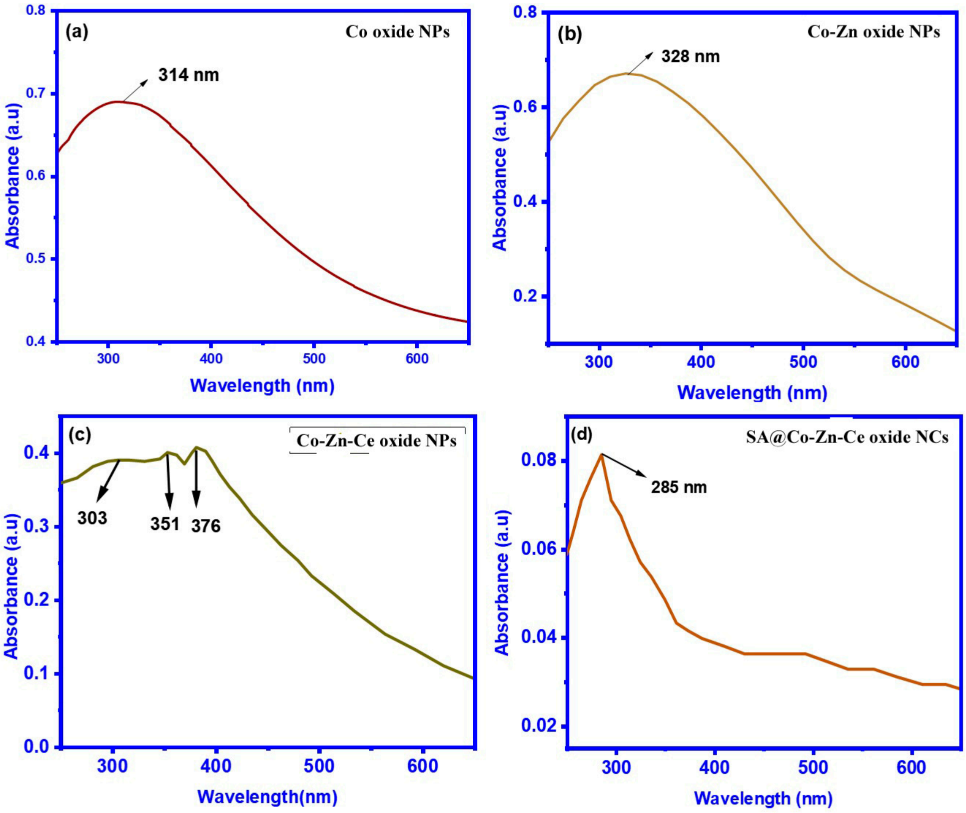

Figure 1. UV-vis absorption spectra of (**a**) Co NPs, (**b**) Co–Zn oxide NPs, (**c**) Co–Zn–Ce oxide NPs, and (**d**) SA@Co–Zn–Ce oxide NCs.

2.2. FTIR

The FTIR spectrum (Figure 2a) of *O. sanctum* exhibits a peak at 3390 cm^{-1}, representing the hydroxyl bond and confirming the presence of phenolic constituents in the extract [28]. Peaks at 2900 cm^{-1} and 2840 cm^{-1} correspond to the stretching vibrations of C-H in aliphatic hydrocarbons. A peak at 2112 cm^{-1} confirms the C≡C of alkynes. The peak at 1970 cm^{-1} shows C=O stretching vibrations of carboxylic acid. The peak at 1620 cm^{-1} confirms the C=C bonds regarding the cyclic aromatic structure. The peak at 1437 cm^{-1} confirms the carbon–carbon bond, while the peak at 1020 cm^{-1} indicates the carbon–nitrogen bond of aliphatic amines found in the extract.

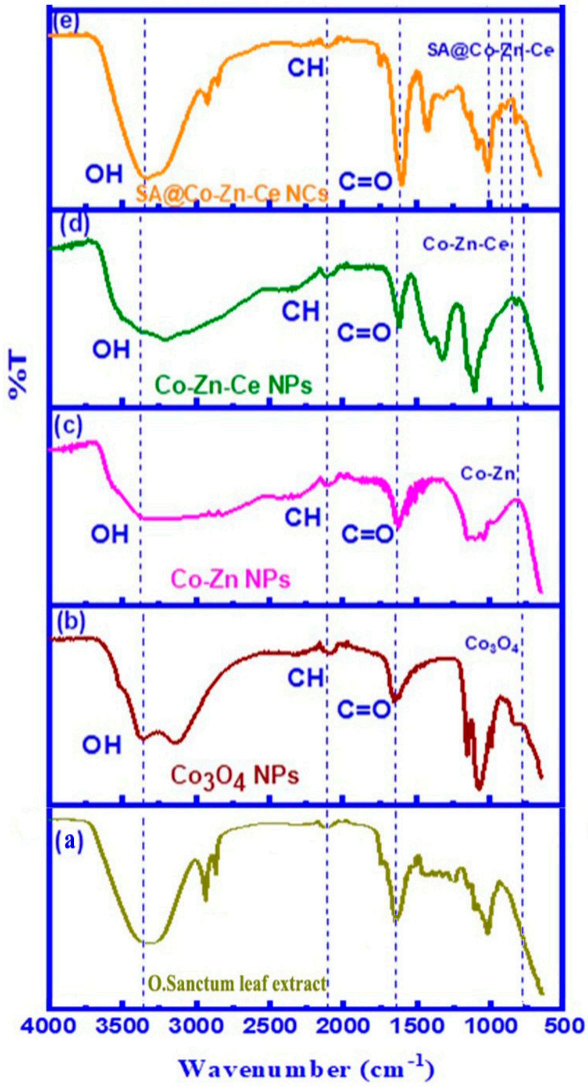

Figure 2. FTIR results: (**a**) Leaf extract of *Ocimum Sanctum*, (**b**) Co oxide NPs, (**c**) Co−Zn oxide NPs, (**d**) Co–Zn–Ce oxide NPs, and (**e**) SA@CoZn–Ce NCs.

The FTIR spectra of synthesized nanoparticles are shown in Figure 2b–d. Cobalt oxide nanoparticles synthesized by reducing *O. sanctum* showed broad peaks at 3132.8 cm^{-1} and 3356.47 cm^{-1}, confirming the presence of the hydroxyl group or water absorbed by nanoparticles during synthesis. Peaks at 2253 cm^{-1}, 2342 cm^{-1}, and 2515.95 cm^{-1} could be attributed to various functional groups such as C≡N or N–H stretching vibrations. Peaks in the 2000–1650 cm^{-1} range are often related to C=C or aromatic structures of phytoconstituents like alkaloids/flavonoids present in the leaf extract. The absorption in the range of 1100–900 cm^{-1} is due to the C–O group, while the peak in the lower-wavenumber region, such as 800 cm^{-1}, could be associated with cobalt oxide nanoparticles [29,30].

The interaction of metal ions of Co–Zn oxide NPs with various functional groups resulted in minor displacement in the peaks of the FTIR spectrum of *O. sanctum* Co NPs. Peaks at 3324 cm^{-1}, 2885 cm^{-1}, 2120.9 cm^{-1}, 1869 cm^{-1}, 1772 cm^{-1}, 1653 cm^{-1}, and 1039 cm^{-1} confirm that some biomolecules from the extract were attached to the surface of NPs, reducing as well as stabilizing these Co–Zn oxide NPs. The lower-wavenumber region, such as 1039 cm^{-1}, is associated with the *O. sanctum* Co–Zn oxide NPs [26,29].

In the FTIR spectra of *O. sanctum* Co–Zn–Ce oxide NPs, a broad peak in the high-wavenumber range, like 3199 cm^{-1}, is often associated with hydroxyl groups, like those found in water molecules. The peak at 1718 cm^{-1} confirms the carbonyl group (C=O stretch), indicative of a ketone or aldehyde functional group. The peaks in this region (1319 cm^{-1}, 1405 cm^{-1}, and 1615 cm^{-1}) could indicate organic functional groups, possibly related to organic molecules on the surface of the metal oxides. Peaks at 1103 cm^{-1}, 1149 cm^{-1}, and 1209 cm^{-1} may also correspond to vibrational modes of C–O stretching. Peaks around 818 cm^{-1} and 1043 cm^{-1} are associated with vibrations of specific chemical bonds related to cobalt/zinc oxides [31].

In the FTIR spectrum of the SA@Co–Zn–Ce oxide nanocomposite, the broad peak in the high-wavenumber region is often associated with O-H stretching vibrations or the presence of the OH group of sodium alginate. The peak at 1742 cm^{-1} suggests the presence of C=O stretching, which is indicative of a ketone or aldehyde functional group also found in sodium alginate. Peaks in the 2000–3000 cm^{-1} range (2038 cm^{-1}, 2107 cm^{-1}, 2853 cm^{-1}, and 2924 cm^{-1}) might be due to vibrations like C-H of hydrocarbons. Peaks at 820 cm^{-1} besides 939 cm^{-1} correspond to metal oxides and functional groups in sodium alginate [32]. The appearance of new peaks or changes in the intensity of existing peaks in specific spectral regions (e.g., below 1000 cm^{-1} for metal–oxygen bonds) indicates chemical interactions and bonding among Co–Zn–Ce oxides. By analyzing these changes in the FT-IR spectra, it can be inferred that the Co-Zn-Ce NPs are chemically linked through covalent bonds, rather than being a physical mixture of functionalized CoO, ZnO, and CeO_2. In the case of SA@Co–Zn–Ce, the FT-IR spectrum likely shows shifts in peak positions, changes in peak intensities, and the appearance of new peaks. These spectral changes indicate the formation of a composite material with strong interactions within the Co–Zn–Ce NPs and with the sodium alginate.

2.3. PXRD Analysis

XRD was employed to analyze the phase distribution and crystalline structure of the obtained nanoparticles and nanocomposites. The XRD results of Co oxide NPs, Co–Zn oxide NPs, Co–Zn–Ce NPs, and the Co–Zn–Ce oxide nanocomposite are presented in Figure 3. The XRD pattern of Co-containing material reveals distinct characteristic peaks located at angles of 31°, 36°, 44°, and 55°, corresponding to the crystallographic planes 220, 311, 400, and 422 of Co_3O_4, respectively (JCPDS Card No. 09-0418).

In the diffractogram of Co–Zn oxide NPs, ZnO is identified by peaks located at $2\theta = 47$, 56, and 62°, indexed as 102, 110, and 103 diffraction lattice planes, respectively (JCPDS card no. 80–0075). Between 30 and 40°, there is a possibility of peak superimposition corresponding to the 100 and 101 planes, similar to those of Co_3O_4. In the XRD pattern for Co–Zn–Ce oxide NPs, cerium oxide shows peaks at 28° and 69°, corresponding to the crystallographic planes 111 and 400 (JCPDS no. 81-0792). Additionally, there may be superimposition at 47° of the peak from the 220 plane with the ZnO peak mentioned above. The XRD pattern of the SA@Co–Zn–Ce oxide nanocomposite indicates a polycrystalline structure, showing a diffraction peak of low intensity of sodium alginate at $2\theta = 22°$. The Scherrer equation was used to determine the average particle size:

$$D = k\,\lambda/\beta\,\cos\theta$$

where D represents the average particle size, k is a constant, λ denotes the wavelength of the X-ray source (0.154 nm), θ indicates the peak position, and β represents the full-width at half-maximum (FWHM) in radians. The average particle sizes of the prepared cobalt oxide, Co–Zn oxide NPs, Co–Zn–Ce oxide, and SA@Co–Zn–Ce oxide nanocomposite were 17.65 nm, 17.36 nm, 16.87 nm, and 15.43 nm, respectively.

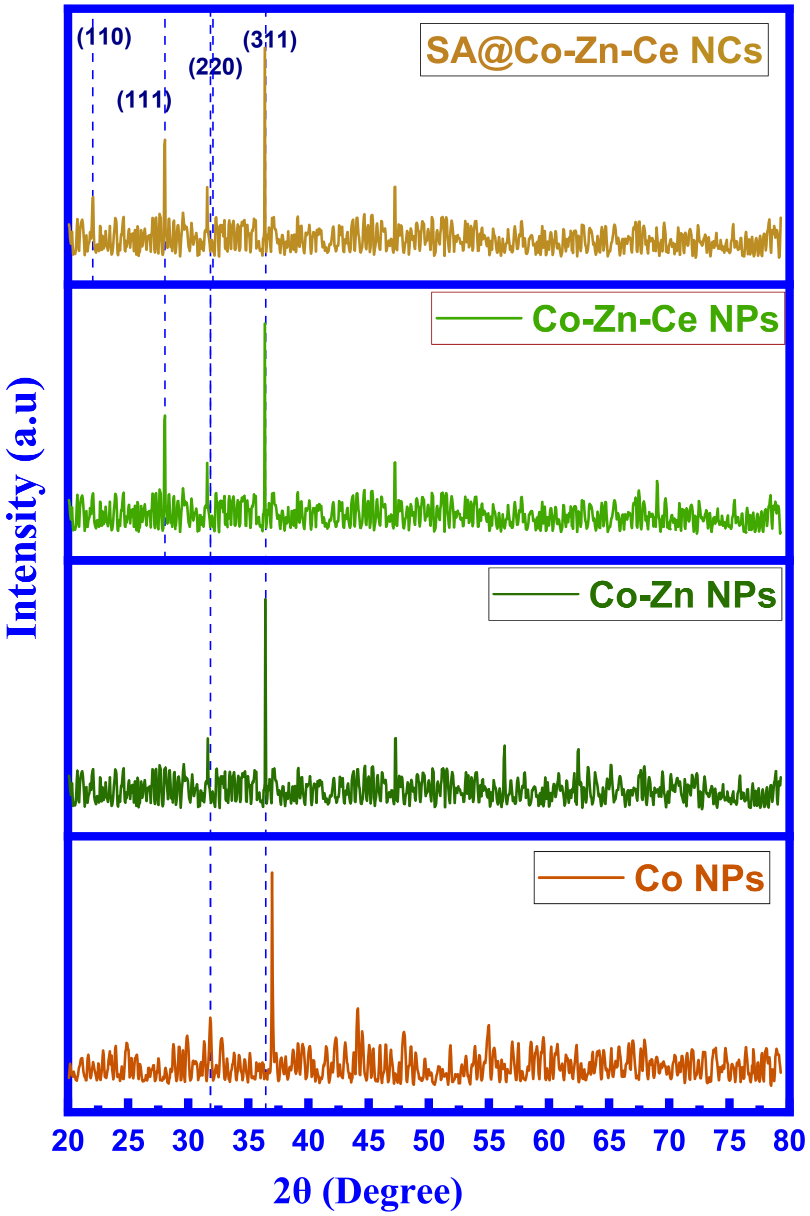

Figure 3. X-ray diffractograms of Co oxide NPs, Co–Zn oxide NPs, Co–Zn–Ce oxide NPs, and SA@Co–Zn–Ce oxide NCs.

2.4. FE-SEM and EDX Analysis

SEM analysis was carried out to observe the influence of sodium alginate incorporation on the morphology of Co–Zn–Ce oxide NPs. SEM micrographs of Co–Zn–Ce oxide and SA@ Co–Zn–Ce are depicted in Figure 4a–d. Concerning Co–Zn–Ce NPS, some cerium oxides appear as a dispersed rod-like strand. In contrast, others seem submerged in the clusters of cobalt–zinc oxide, and this non-uniformity comes from agglomeration. These clusters can result from attractive forces between the nanoparticles, such as van der Waals forces, which cause them to stick together. The agglomerates of Co–Zn–Ce nanoparticles appear compact and dense in SEM images, with a minimal spacing between individual particles. This compactness can lead to a high particle density within the agglomerates.

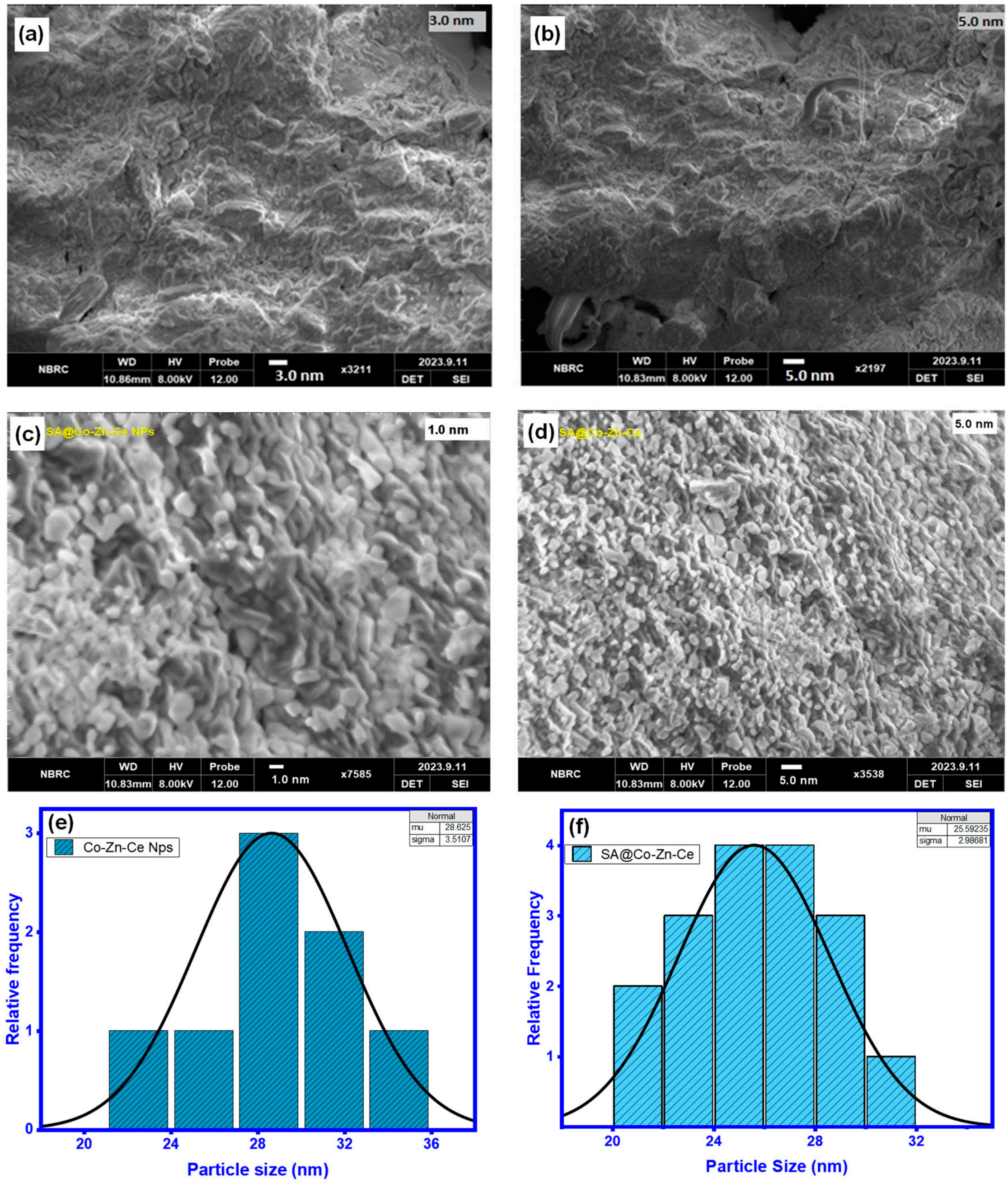

Figure 4. SEM micrographs of (**a**,**b**) Co–Zn–Ce oxide NPs and (**c**,**d**) SA@Co–Zn–Ce oxide NCs. Average size distribution of (**e**) Co–Zn–Ce oxide NPs and (**f**) SA@Co–Zn–Ce oxide NCs.

On the other hand, in the SEM images of SA@Co–Zn–Ce oxide, some nanoparticles of Co–Zn–Ce oxides may be located on the surface of the beads, creating a rough texture. In contrast, others may be partially embedded within the bead matrix. The SA@Co-Zn-Ce oxide composite beads exhibit irregular spherical shapes, and these irregularities can result from the immobilized nanoparticles, which have modified the shape of the original SA beads. The size distributions of Co–Zn–Ce oxide NPs and SA@Co–Zn–Ce oxide NCs are shown in Figure 4e,f, characterized by peaks centered at 28 nm and 25 nm, respectively. Co–Zn–Ce nanoparticles have an average particle size of 28.62 nm, and the SA@Co–Zn–Ce nanocomposite has an average particle size of 25.59 nm, with a grain size range of 20 to 35 nm. SEM micrographs show larger particle sizes than the XRD data, indicating that each particle is likely composed of many aggregated crystallites or grains, which contributes to the observed size disparity.

An energy-dispersive X-ray (EDX) spectrum (see Figure 5a) was collected from the Co–Zn–Ce oxide NP sample used during the SEM examination, as shown in Figure 4. From Figure 5a, it is clear that peaks corresponding to cobalt (Co), zinc (Zn), and cerium (Ce) are present. The atomic percentages (at. %) of these elements were determined to be 13.08% (Co), 16.9% (Zn), 46.05% (Cu), and 87.5% (O). The prominent oxygen peak confirms that the sample is a metal oxide. The EDX analysis indicated that no other elements were detected, confirming the purity of the Co-Zn-Ce oxide NPs and the absence of surfactants or other impurities.

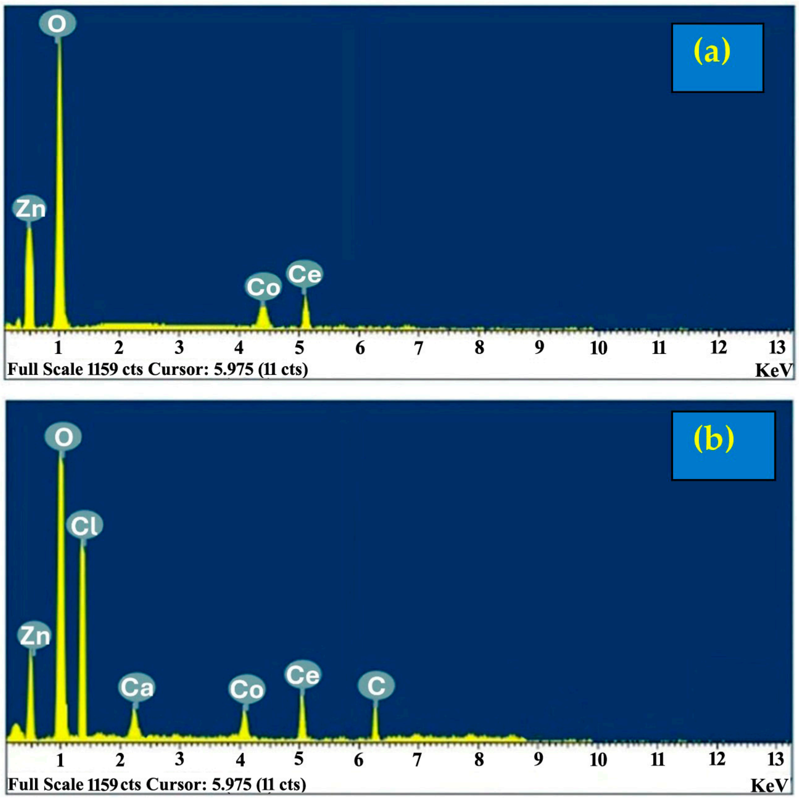

Figure 5. EDX results of (**a**) Co–Zn–Ce oxide NPs and (**b**) SA@Co–Zn–Ce oxide NCs.

In contrast, an EDX spectrum of the SA@Co–Zn–Ce oxide nanocomposite (NC) sample, shown in Figure 5b, revealed the presence of calcium (Ca) and chlorine (Cl) peaks. These peaks are attributed to sodium alginate in the SA@Co–Zn–Ce oxide NCs. The calcium peaks suggest gel structure formation, where calcium ions link with the alginate chain. Meanwhile, the chlorine peaks, likely from residual sodium chloride (NaCl), affect ionic strength and stability without influencing gel formation. The atomic percentages in this sample were 10.08% (Co), 46.05% (Zn), and 80.9% (O). The lower intensity of the Ca peak, compared to Co, Zn, and Ce, indicates a smaller amount of calcium, consistent with sodium alginate acting as a support rather than a major component. These findings support the application of Co–Zn–Ce oxide NPs in metallic coatings.

2.5. XPS Analysis

The photocatalytic performance of photocatalysts is significantly influenced by their surface chemical state. In this study, X-ray photoelectron spectroscopy (XPS) was utilized to determine the oxidation state and chemical composition of the SA@Co-Zn-Ce oxide photocatalysts. The results, presented in Figure 6a,b, show peaks at 779.80, 794.97, 121.79, and 144.83 eV, corresponding to Co $2p_{3/2}$, Co $2p_{1/2}$, Zn $2p_{3/2}$, and Zn $2p_{1/2}$, respectively [33]. Additionally, the presence of Ce oxide NPs is confirmed by five peaks in the Ce 3d spectrum (Figure 6c) at binding energies of 882.19, 888.10, 897.43, 900.40, and 903.21 eV, originating from Ce 3d$_{5/2}$ and Ce 3d$_{3/2}$ [33]. The peak at a binding energy of 529.76 eV (Figure 6f) is attributed to O 1s in metal oxides, validating the presence of tri-metal oxides.

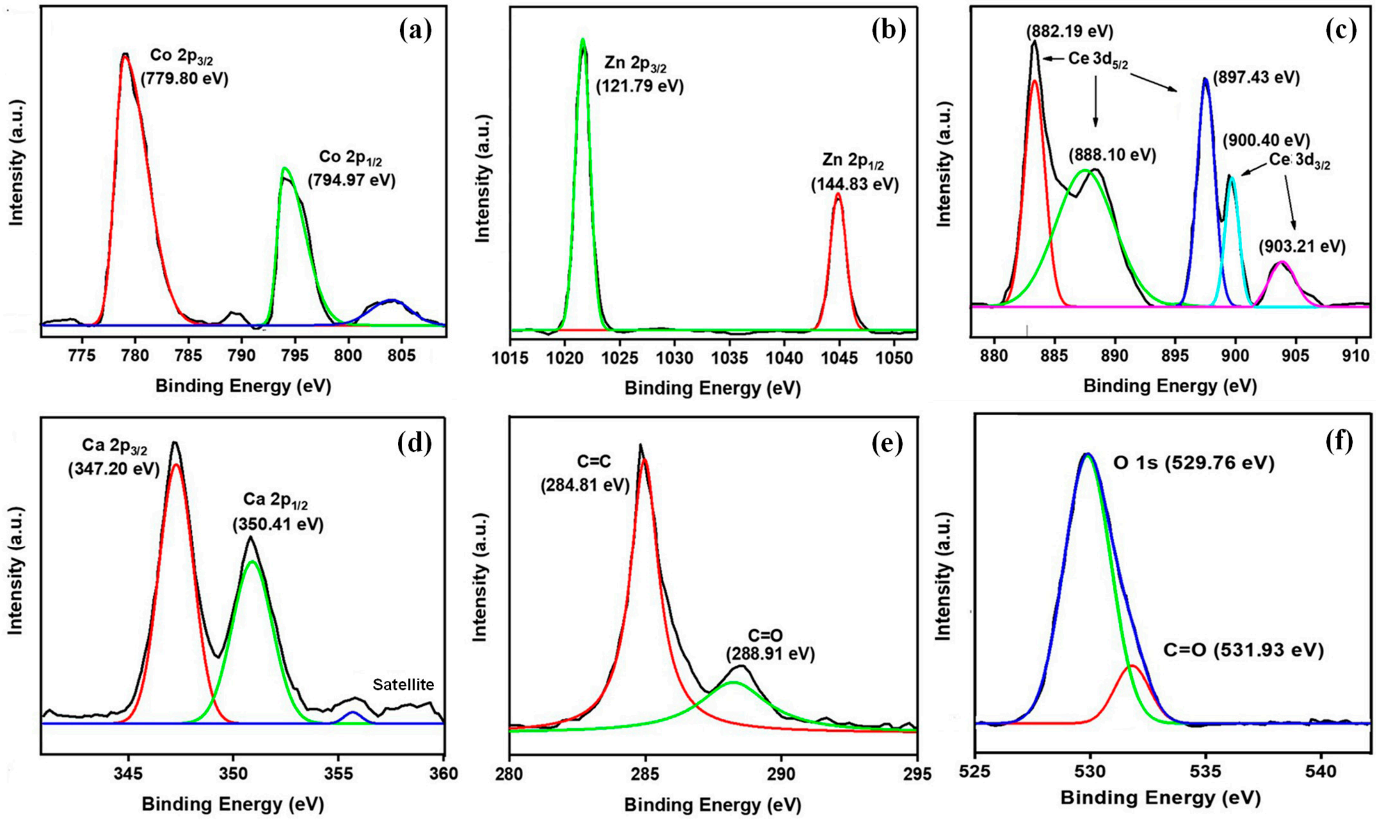

Figure 6. XPS spectra of (**a**) Co 2p, (**b**) Zn 2p, (**c**) Ce 3d, (**d**) Ca 2p, (**e**) C 1s, and (**f**) O 1s of as SA@Co-Zn-Ce oxide NCs. The colored lines represent the peak deconvolution.

The formation of SA@Co-Zn-Ce oxide NCs is further supported by the peaks at binding energies of 347.20 and 350.41 eV, attributed to Ca 2p3/2 and Ca 2p1/2, and the peaks at 284.81 and 288.91 eV, corresponding to C=C and C=O groups in alginate molecules, as shown in Figure 6d–f. Additionally, the presence of a second peak in the O 1s spectrum (Figure 6f) at a binding energy of 531.93 eV is attributed to C=O groups in alginate molecules [33]. These XPS results confirm the synthesis of SA@Co-Zn-Ce oxide NCs and the incorporation of alginate molecules, indicating strong interactions between the metal oxides and the alginate support.

2.6. Zeta Potential

The evaluation of the zeta potential of Co–Zn–Ce oxide and sodium alginate-anchored Co–Zn–Ce oxide reveals significant differences in their surface charge characteristics (Figure 7). The Co–Zn–Ce oxide material exhibits a zeta potential of −2.07 mV, signifying a surface with a slight negative charge. In contrast, when sodium alginate is used to anchor Co–Zn–Ce oxide, the zeta potential dramatically shifts to −12.28 mV, indicating a highly negatively charged surface. This substantial change in zeta potential highlights the successful anchoring of sodium alginate and the alteration of the surface charge properties, which can have important implications for applications involving these materials in various contexts. This change in zeta potential value indicates that the metal oxides entrapped in sodium alginate exhibit greater stability compared to the metal oxides alone [34].

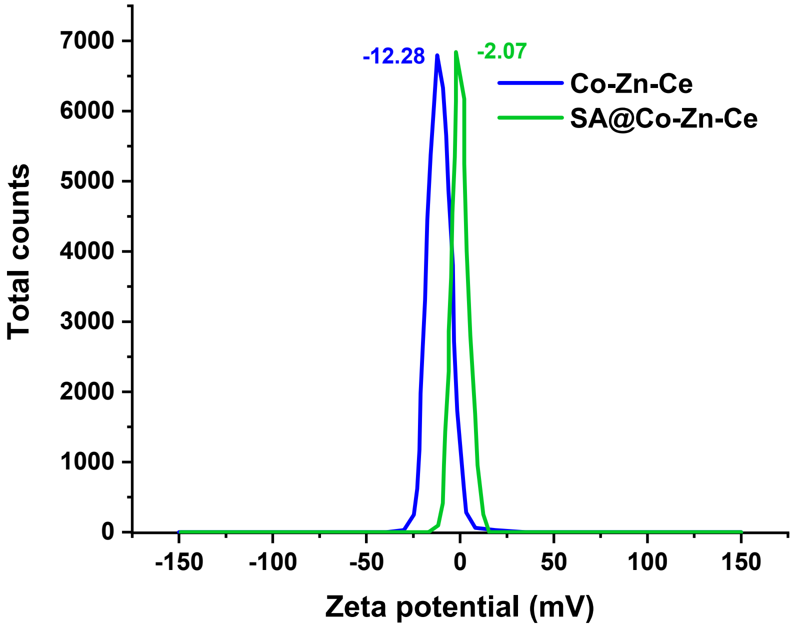

Figure 7. Zeta potential of Co−Zn−Ce oxide NPs and SA@Co−Zn−Ce oxide.

2.7. DLS

The DLS method was utilized to measure the particle size of the SA@Co–Zn–Ce oxide nanocomposite with the Zetasizer. Through the application of this technique, the nanocomposite was evaluated for the polydispersity index (PDI), size distribution (SD), and average particle size (APS), with the results presented in Figure S2. The measurements indicate an average size of approximately 81 nm. The PDI for the SA@Co–Zn–Ce oxide is 0.87 [34,35]. The increased size of the SA@Co–Zn–Ce oxide nanocomposite is attributed to the presence of a water layer enveloping the nanoparticle surfaces, influencing the hydrodynamic diameter measurement. The water layer adds to the overall measured size by contributing to the apparent dimensions of the nanoparticles.

2.8. N_2 Adsorption at −196 °C

The synthesized Co-Zn-Ce NPs and SA@Co–Zn–Ce oxide nanocomposite were characterized by the adsorption of N_2 at −196 °C. Figure 8a,b show the respective isotherms. The adsorption–desorption plots show type IV isotherms, which are characteristic of mesoporous materials. The BET surface areas of the Co–Zn–Ce oxide nanoparticles (NPs) and the SA@Co–Zn–Ce oxide nanocomposite are 167.346 and 24.14 m^2/g, respectively. Their average pore diameters were determined to be 34.6 and 9.3 Å, respectively, through Barrett–Joyner–Halenda (BJH) analysis, as depicted in Figure 8(c, d), confirming their mesoporous nature [36]. These findings highlight the reduced pore volume and mesoporous structure of the SA@Co–Zn–Ce oxide nanocomposite, which can serve as a versatile host for a range of applications. This is particularly relevant in the photocatalytic degradation of the RR24 dye [37,38].

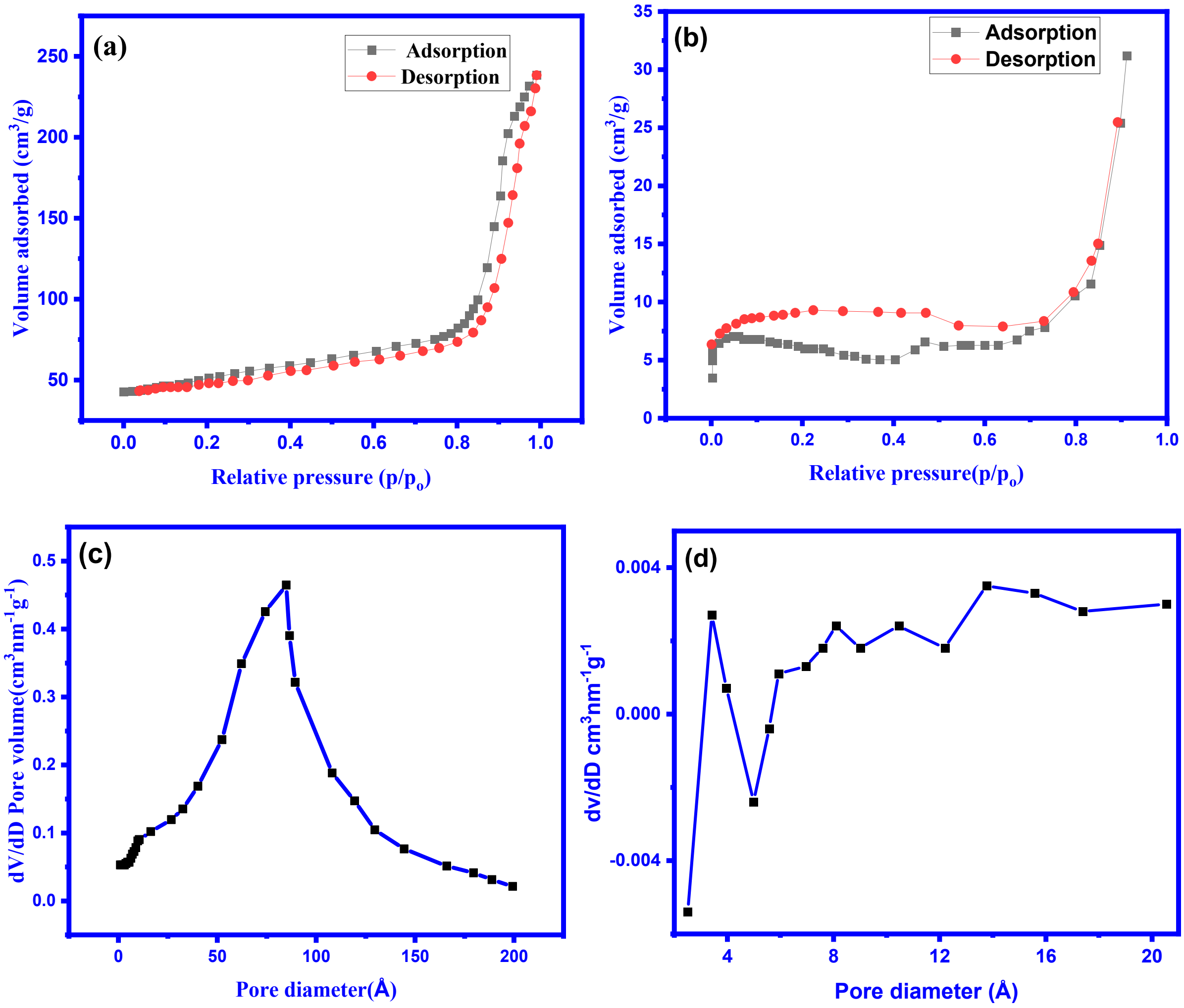

Figure 8. (**a**,**b**) Adsorption–desorption isotherms for Co−Zn−Ce oxide NPs and SA@Co−Zn−Ce oxide NCs. (**c**,**d**) BJH pore size distribution for Co−Zn−Ce oxide NPs and SA@Co−Zn−Ce oxide NCs.

2.9. Antioxidant Potential

The antioxidant activity of Co NPs, Co–Zn NPs, Co–Zn–Ce oxide NPs, and the SA@Co–Zn–Ce oxide nanocomposite produced from *O. sanctum* extract was evaluated via the free radical DPPH scavenging assay. Results are shown in Table S1. The primary mechanism of antioxidant action is electron transfer, which also causes the solution color to shift from purple to pale yellow. The general reaction of DPPH with antioxidants is illustrated in Figure 9. The formation of a stable DPPH molecule involves the attainment of electrons or hydrogen from Co oxide NPs, Co–Zn oxide NPs, Co–Zn–Ce oxide NPs, and the SA@Co–Zn–Ce oxide composite. After analyzing the samples at various concentrations (50, 75, and 100 µg/mL), it was found that the proportion of DPPH free radicals was more scavenged when the quantities of the materials were increased. When these NPs and nanocomposite interacted with DPPH, they released electrons, which caused the absorbance to decline and the color to shift from purple to pink. As depicted in Figure 10, the results indicated that the samples showed significant free radical inhibitory effects, specially at a concentration of 100 µg/mL. At that concentration, the maximum percentages of DPPH free radical scavenging for Co NPs, Co–Zn NPs, Co–Zn–Ce oxide NPs, and the SA@Co–Zn–Ce composite were 78%, 81.31%, 88.44%, and 89.31%, respectively. Among all oxide samples, the final product, SA@Co–Zn–Ce oxide NCs, demonstrated the highest DPPH free radical scavenging potential.

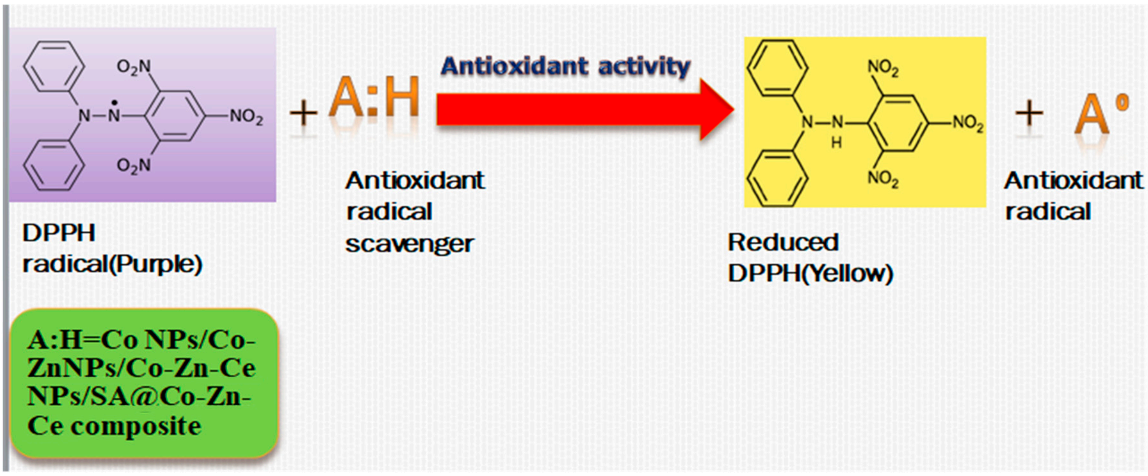

Figure 9. Proposed mechanism for antioxidant activity via free radical DPPH scavenging assay.

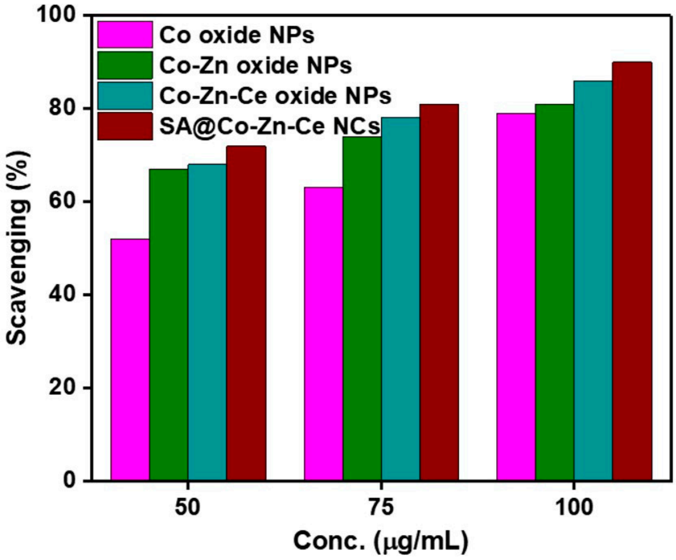

Figure 10. % Scavenging of DPPH radicals by Co NPs, Co–Zn oxide NPs, Co–Zn–Ce oxide NPs, and SA@Co–Zn–Ce oxide composite.

2.10. Photocatalytic Degradation of RR24

The SA@Co–Zn–Ce oxide nanocomposite was used as a photocatalyst to degrade RR24 dye. The assessment of λ max (532 nm) for RR24 is shown in Figure S3. Figure 11a reveals that the degradation of RR24 by photolysis was only 16% in 20 min, 9% by adsorption in the dark, and 55% by photocatalysis at the same time. The photocatalytic degradation of RR24 dye using SA@Co–Zn–Ce oxide was tracked through UV–vis spectroscopy, focusing on the absorption bands at 532 nm and 280 nm (see Figure 11b). When SA@Co–Zn–Ce oxide was added and exposed to sunlight, a noticeable reduction in the intensity of these absorption bands was observed (see Figure 11b). The average sunlight flux, measured with a pyranometer, was approximately 645 W/m^2. It can be easily observed that the absorption of RR24 dye decreases with time because of photocatalytic degradation by the SA@Co–Zn–Ce oxide catalyst. The disintegration of aromatic rings of reactive red 24 dye was considered responsible for the steady decrease in the absorbance peak over time [35,36]. Figure S4 illustrates the factors that were effective on photocatalytic degradation (concentrations of catalysts, H_2O_2 and dye, pH, and temperature). Table 1 compares several catalysts for the degradation of RR24 dye, showing that our composite is very effective.

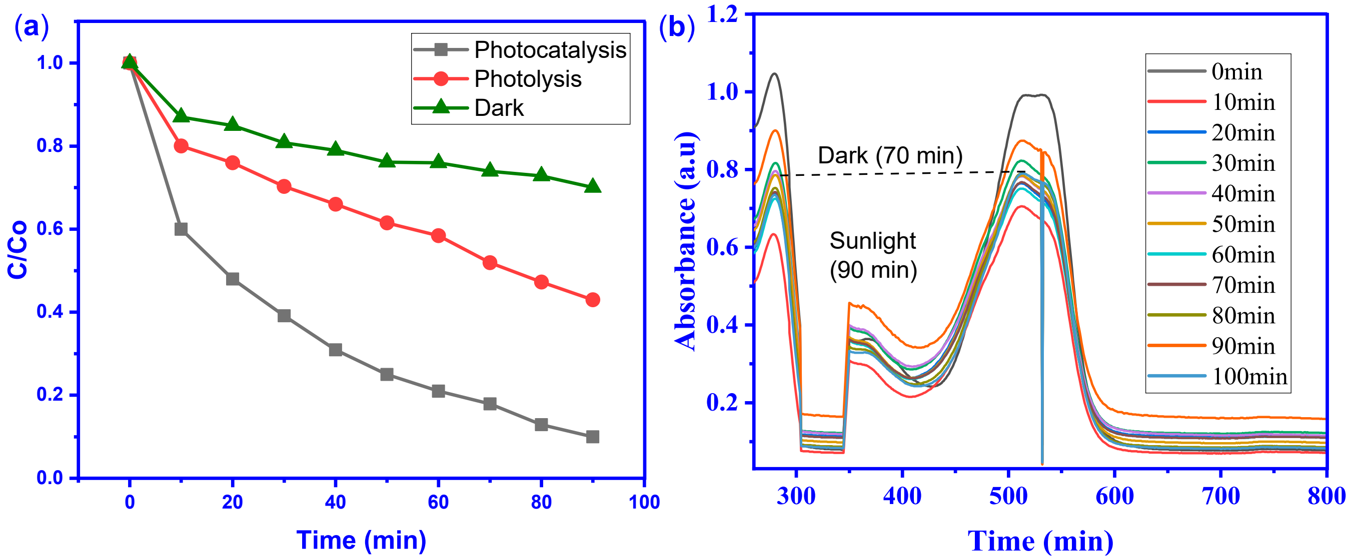

Figure 11. (**a**) Normalized absorbance of dye under dark conditions and sunlight (illustrating the effects of photolysis and photocatalysis) and (**b**) UV-vis spectral results showing the time-dependent degradation of RR24 dye.

Table 1. Comparison of different photocatalysts for the degradation of RR 24.

Photocatalyst	Time (min)	%Degradation	Light Source	References
$K_6SiW_{11}O_{39}Sn^{II}$ (SiWSn)	180	52	Sunlight	[39]
SBB-ZnO_3 (modified with sugarcane bagasse biochar)	60	85.28	Visible light	[40]
CRHB-ZnO_3 (modified with cassava root husk biochar)	60	75.32	Visible light	[40]
Photo-Fenton reagent	9	76	Visible light	[41]
TiO_2	60	88.69	UV light	[39]
FePc-mBC (iron phthalocyanine-doped millet biochar)	120	93	Visible light	[42]
ultrasound/exfoliated graphite/H_2O_2	120	89.09	Visible light	[43,44]
SA@ Co–Zn–Ce oxide nanocomposite	90	95	Sunlight	Present work

2.10.1. Influence of RR24 Dye Concentration

Experiments focused on how the initial concentration of the RR24 dye influenced its degradation efficiency. To assess the catalyst impact under sunlight, separate experiments were conducted under both dark and sunlight conditions [45]. In the absence of sunlight, when the dye degradation experiment was performed with the catalyst, a minimal reduction in absorbance was observed (Figure 12). This highlights the dependency of dye degradation efficiency on the presence of both SA@Co–Zn–Ce oxide NCs and sunlight. The results of comparing various initial RR24 dye concentrations (5–15 ppm) are depicted in Figure 12. It can be seen that with an increase in the concentration of RR24 dye, a greater number of dye particles adhered to the photocatalyst surface. This increased particle presence led to a reduction in the generation of active sites during the reaction, as it obstructed the passage of light [39]. Consequently, the efficiency of the SA@Co–Zn–Ce oxide NC photocatalyst notably diminished due to the limited availability of active sites.

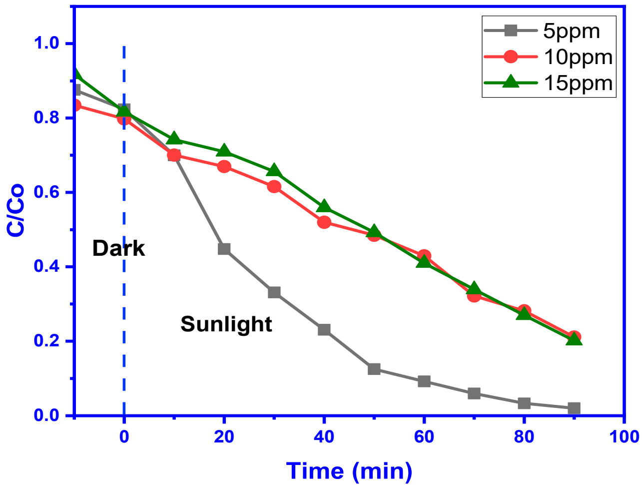

Figure 12. The absorbance of dye in the dark and sunlight in the presence of catalyst; 5 ppm–15 ppm of SA@ Co–Zn–Ce oxides at 30 °C.

2.10.2. Influence of pH

The pH of the dye solution is another crucial factor that significantly influences dye degradation. Varying the pH value affects the chemical characteristics of the photocatalyst as well as the RR24 dye utilized for degradation. Since RR24 dye is an anionic dye, it exhibited maximum degradation at acidic pH levels due to a higher concentration of hydrogen ions [46,47]. In other words, SA@Co–Zn–Ce oxide could potentially exhibit a much higher efficiency in an acidic medium due to the greater adsorption of the anionic dye over the catalytic surface. When the dye degradation experiment was performed without sunlight but with the catalyst, a slight decrease in absorbance was noted (Figure 13). This demonstrates that the effectiveness of dye degradation hinges on the concurrent presence of both SA@Co–Zn–Ce oxide NCs and sunlight. At a pH value of 3, the color of the RR24 dye faded almost completely. The percentage efficiency of the photocatalyst at different pH values is depicted in Figure 13.

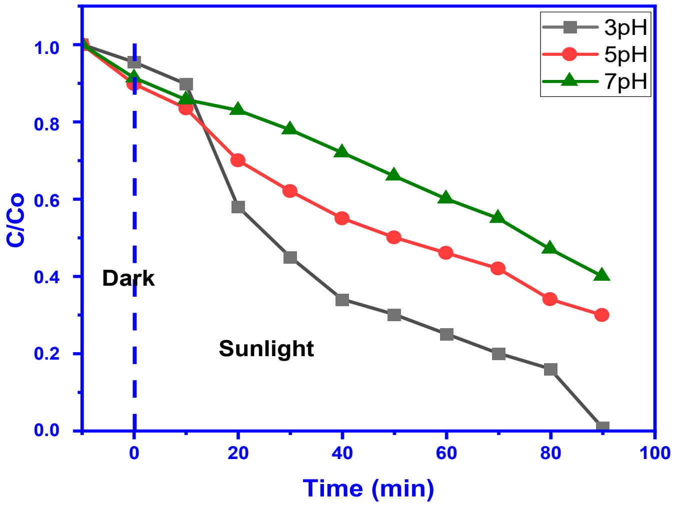

Figure 13. Variation in absorbance of dye with time in both dark and sunlight at pH 3, 5, and 7 (5 ppm dye solution; 15 mg of SA@ Co–Zn–Ce oxide NCs at 30 °C).

2.10.3. Influence of Temperature

In the absence of sunlight, with the catalyst present, a slight decrease in absorbance was observed during the dye degradation experiment (Figure 14). This indicates that the efficacy of dye degradation is reliant on the presence of both SA@Co–Zn–Ce oxide NCs and sunlight.

The obtained results show that at 20 °C, a reduced desorption of dye particles is inevitable, minimizing the reaction, as seen in the literature [48]. On the other hand, as the temperature is raised to 40 °C, the adsorption of dye particles on the catalyst is also no longer preferred, which restricts the degradation reaction, as reported elsewhere [40,44]. Hence, higher temperatures reduce the efficiency of photocatalysts. Temperature optimization favors efficient photocatalytic degradation. According to the findings in Figure 14, particles of dye are more likely to bind to the surface of the SA@Co–Zn–Ce oxide NC catalyst at a temperature of about 30 °C, as also seen by other authors [44].

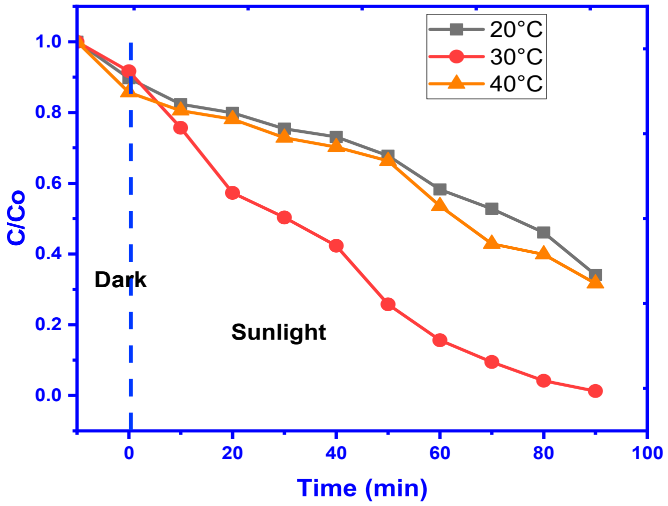

Figure 14. Effect of temperature (both dark and sunlight) on % degradation at pH 5 (5 ppm dye solution; 15 mg of SA@ Co–Zn–Ce oxide NCs).

2.10.4. Effect of Concentration of SA@ Co–Zn–Ce Oxide NC Photocatalyst Dose

As the amount of catalyst increases, a greater number of active sites are generated on the catalytic surface [47]. When the dye degradation experiment was conducted in the dark with the catalyst, a modest reduction in absorbance was observed (Figure 15). This underscores that the effectiveness of dye degradation depends on the presence of both SA@Co–Zn–Ce oxide NCs and sunlight. The results are presented in Figure 15, and the degradation efficiency decreased after 20 mg because the excess catalyst blocked the passage of light. As a result, 20 mg was chosen as the ideal catalyst dosage.

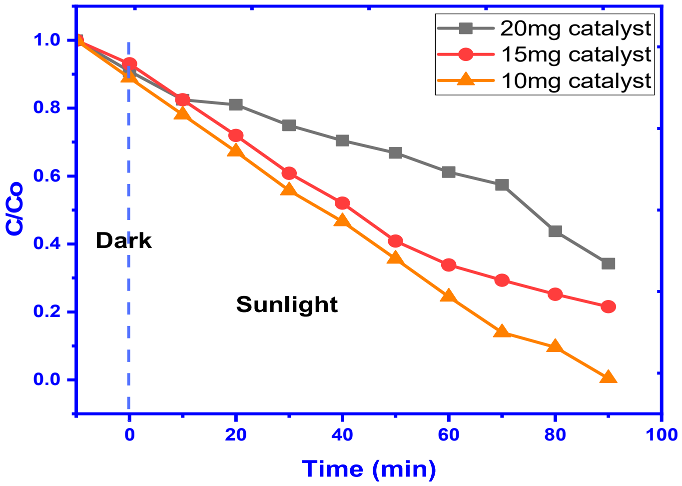

Figure 15. Effect of concentration of SA@ Co–Zn–Ce oxide NCs on % degradation in both dark and sunlight at pH 5 in 5 ppm dye solution.

2.10.5. Influence of H_2O_2 Concentration

Hydrogen peroxide (a green oxidant) is one of the most popular oxidizing agents. It was used to improve the generation of ·OH radicals during the reaction to enhance the photocatalytic degradation. It competes with other species for electrons when added to the reaction mixture. However, because hydrogen peroxide is a powerful agent, the likelihood of electrons being grabbed by this substance is increased. As a result, the degradation rate increases while the phenomenon of electron–hole recombination decreases [47,49]. The results of Figure 16 reveal that introducing hydrogen peroxide improves the efficiency of photocatalysis and reduces the time and sunlight needed for color removal. To evaluate the catalyst impact individually under sunlight, control experiments were performed under both dark and sunlight conditions, as in previous cases. In the absence of sunlight, with the catalyst present, a minimal change in absorbance was observed during the dye degradation experiment (Figure 16). This highlights the critical role of both SA@Co–Zn–Ce oxide NCs and sunlight in enhancing photocatalytic activity.

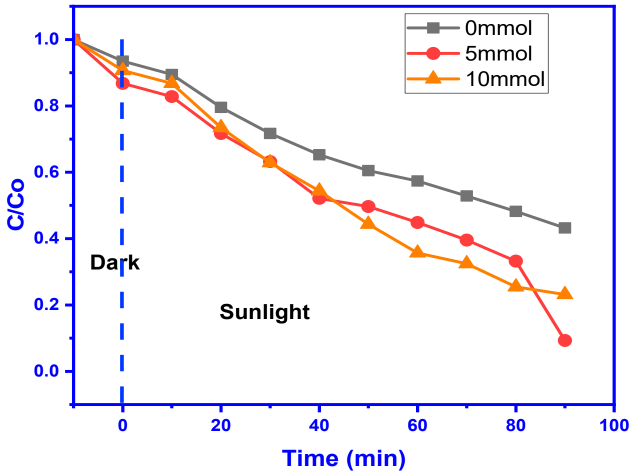

Figure 16. The effect of H_2O_2 on degradation with time in both dark and sunlight.

2.10.6. Recyclability of SA@Co–Zn–Ce Oxide NC Photocatalyst

For practical applications to be possible, an effective photocatalyst must display chemical stability and recyclability. The degrading efficacy of SA@Co–Zn–Ce oxide NCs decreased from 95% in the initial cycle to 80% in the fourth cycle, as shown in Figure 17. This fact reveals its amazing catalytic potential because of its good stability and crystalline nature. It was observed that during the recovery processes, a portion of the catalyst was washed away, slightly diminishing the photocatalytic effectiveness. However, the remarkable reusability demonstrated that SA@Co–Zn–Ce oxide NCs remain an effective photocatalyst for practical applications.

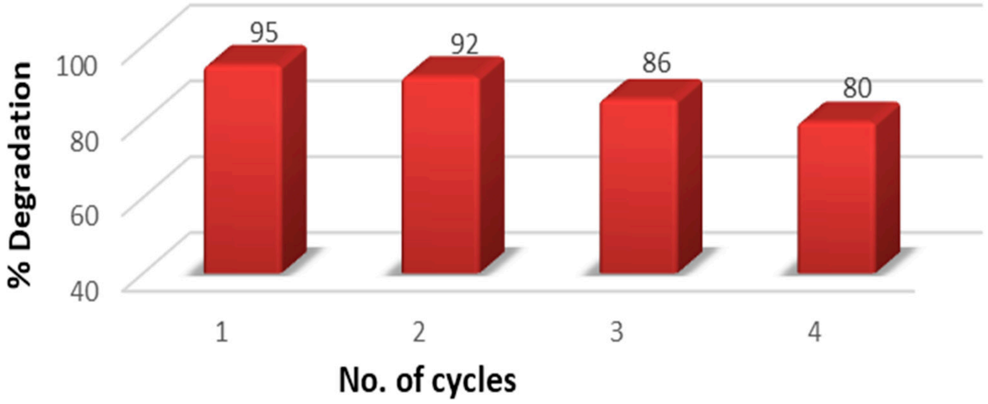

Figure 17. Recycling efficiency of SA@Co-Zn-Ce oxide NCs.

2.10.7. Effect of Scavengers

The influence of scavengers on the photodegradation of RR24 dye was investigated using sodium sulfate (Na_2SO_4), sodium chloride (NaCl), and sodium carbonate ($NaHCO_3$) during a 90 min irradiation period, as depicted in Figure 18. NaCl exhibited notable inhibition (65%) by scavenging photogenerated holes, thereby generating OH radicals. Similarly, Na_2SO_4 (72%) and $NaHCO_3$ (80%) scavenged holes through reactions with hydroxyl ions and by producing carbonate radicals [45].

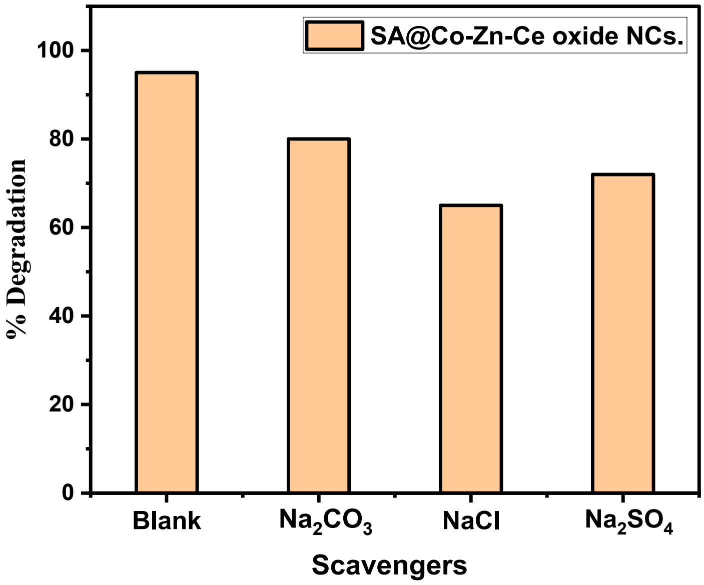

Figure 18. Effect of scavengers on the degradation of RR24 by SA@Co–Zn–Ce NCs.

2.10.8. Photocatalytic Degradation Mechanism of RR24

Figure 19 depicts the mechanism of the photocatalytic degradation of RR24 dye. Valence band (VB) electrons in SA@Co–Zn–Ce oxide NPs become excited and move in the direction of the conduction band (CB) once they are subjected to sunlight. The Schottky barrier, created at the interface by the presence of cobalt, zinc, and cerium metals as active centers, inhibits electrons and holes from rapidly recombining. In addition, the holes formed in the VB of SA@Co–Zn–Ce oxide NPs destroy the RR24 dye molecules through direct contact or by the production of hydroxyl radicals through the oxidation of H_2O molecules. Co, Zn, and Ce metal ions serve as a Schottky barrier and facilitate the promotion of electrons for surface plasmon resonance, which activates the production of reactive oxygen species, such as the O_2^- radical, leading to the breakdown of the RR24 dye [49].

2.10.9. Kinetic Studies of Photocatalytic Degradation of RR24

The results obtained for the kinetics of RR24 degradation are more closely related to the pseudo-first-order model [50]. In this context, a pseudo-first-order reaction was employed for kinetic assessment, which involves treating a second-order reaction as if it were pseudo-first-order by utilizing a large amount of one reactant to yield more precise outcomes. This approach is beneficial since only one analyte concentration, i.e., RR24, can be precisely measured. Thus, the kinetic studies were evaluated with the pseudo-first-order reaction, which is commonly used to assess azo dyes in previous studies [40,50]. The rate equation for the pseudo-first-order reaction is described below:

$$-\ln (A_t/A_o) = kt$$

where "A_o" signifies the initial absorbance at time t = 0, "A_t" is the absorbance at time t, and "k" denotes the rate constant. Figure S5a,b depict the plots of A_o/A_t vs. time and ln

(A_t/A_o) versus time for 10, 15, and 20 mg of catalyst; Figure S6a,b for 5, 10, and 15 ppm of RR24 dye; and Figure S7a,b for 3, 5, and 7 pH values. Table S2 shows the R^2 values and rate constant k_{obs} (min^{-1}) for the photocatalytic degradation of RR24 dye using the SA@Co–Zn–Ce nanocomposite.

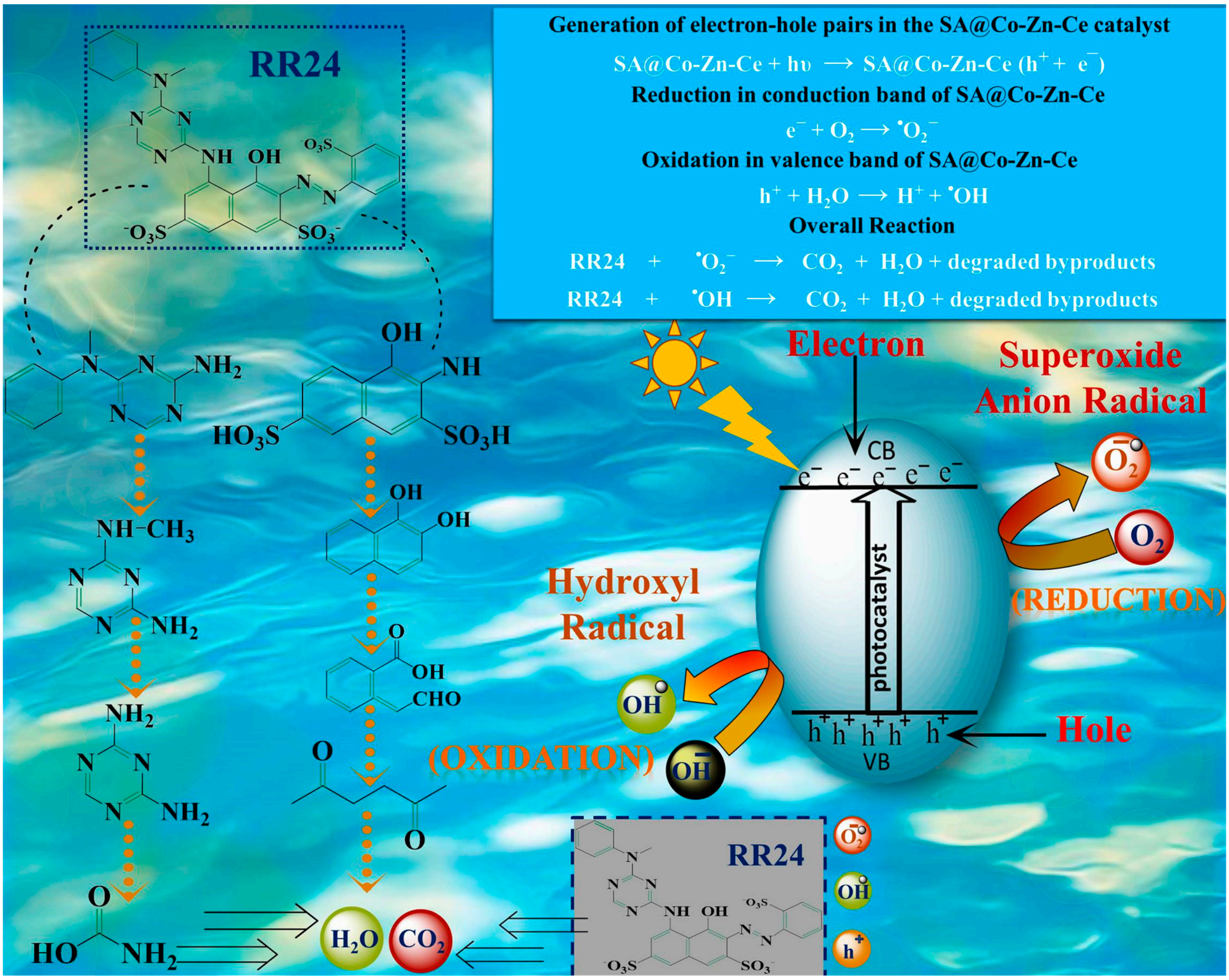

Figure 19. Mechanism of photocatalytic degradation of RR24 dye.

3. Materials and Methods

3.1. Chemicals and Reagents

Cobalt chloride hexahydrate ($CoCl_2{\cdot}6H_2O$, Sigma Aldrich 99%, Taufkirchen, Germany), zinc chloride dihydrate ($ZnCl_2{\cdot}2H_2O$, Sigma Aldrich 99%), ammonium cerium nitrate ($(NH_4)_2[Ce(NO_3)_6]$, Sigma Aldrich 99%), sodium alginate ($NaC_6H_7O_6$, Sigma Aldrich 99%), calcium chloride ($CaCl_2$, Sigma Aldrich 99%), and deionized water (99.99%, PAEC PK, Islamabad, Pakistan) were utilized without further purification. Reactive Red 24 dye ($C_{26}H_{17}ClN_7Na_3O_{10}S_3$, Sigma Aldrich 99%) was employed for degradation. Leaves of the *Ocimum sanctum* (Tulsi) plant were collected from The Islamia University of Bahawalpur, Pakistan.

3.2. Preparation of Tulsi (Ocimum sanctum) Leaf Extract

Fresh leaves of Tulsi were initially washed with distilled water to remove dust particles and then air-dried in darkness for one week. Once dried, the leaves were ground into a fine powder using a mortar and pestle. Next, 20 g of the dried leaf powder was weighed into a conical flask containing 120 mL of deionized water and left to stand for one day. Following this, the mixture was magnetically stirred at 80 °C for 40 min after the initial 24 h period. The resulting solution was then filtered through filter paper to obtain the leaf extract, which was stored for future experiments. The detailed process is illustrated in Figure S8.

3.3. Biosynthesis of Co Oxide NPs

$CoCl_2{\cdot}6H_2O$ was used as a precursor salt for the synthesis of cobalt nanoparticles. A 0.5 M solution of cobalt chloride hexahydrate was prepared in 100 mL of deionized water. Then, 20 mL of *O. sanctum* leaf extract was added dropwise into 30 mL of the cobalt solution and stirred for 2 h at 80 °C. The solution was cooled for 30 min at room temperature. Subsequently, centrifugation was carried out at 6500 rpm for 15 min at 25 °C, and the product was rinsed with distilled water. The cobalt oxides formed were then calcined at 70 °C to obtain fine precipitates. The end product was pulverized into fine particles. The preparation scheme is shown in Figure S9.

3.4. Biosynthesis of Co–Zn Oxide NPs

$ZnCl_2{\cdot}2H_2O$ and $CoCl_2{\cdot}6H_2O$ were used as precursor salts for the fabrication of cobalt–zinc nanoparticles. Separate 0.5 M solutions of zinc chloride dihydrate and cobalt chloride hexahydrate were prepared in deionized water. An amount of 40 mL of *O. sanctum* leaf extract was heated to 80 °C with continuous stirring on a hot plate, and the cobalt chloride hexahydrate solution was added dropwise. After a few minutes, the zinc chloride solution was introduced, and the mixture was kept at 80 °C for 2 h. The suspension was then cooled for 1 h at 25 °C. Centrifugation was carried out at 6500 rpm for 15 min at 25 °C, and the product was washed with deionized water. The nanoparticles were then calcined at 70 °C to obtain a fine precipitate. After drying, the final product was pulverized into fine particles. The process is shown in Figure S10.

3.5. Biosynthesis of Co–Zn–Ce Oxide NPs

Ammonium cerium nitrate was also added along with $CoCl_2{\cdot}6H_2O$ and $ZnCl_2{\cdot}2H_2O$ as a precursor salt for the fabrication of cobalt–zinc–cerium nanoparticles. Separate 0.3 M solutions of ammonium cerium nitrate, zinc chloride dihydrate, and cobalt chloride hexahydrate were prepared in deionized water. An amount of 40 mL of *O. sanctum* leaf extract was heated to 80 °C with continuous stirring on a hot plate, and the cobalt chloride hexahydrate solution was added dropwise. Then, after a few minutes, the solutions of zinc chloride and ammonium cerium nitrate were introduced as well, and the mixture was stirred with heating for 3 h. The suspension was cooled for 1 h at 25 °C. Centrifugation was carried out at 6500 rpm for 15 min at 25 °C, and then the product was rinsed with ethanol. Afterward, the Co–Zn–Ce oxide NPs were calcined at 80 °C. After drying, the product was pulverized into fine particles. The scheme is shown in Figure S11.

3.6. The Reduction Mechanism of Co–Zn–Ce Oxide NPs

The synthesis of Co–Zn–Ce oxide nanoparticles is evidenced by a noticeable color change in the solution, confirming the reduction of metal ions. Upon introduction of the Tulsi (*Ocimum sanctum*) extract, the solution rapidly transitions to a dark brown hue, indicating the formation of Co–Zn–Ce oxide nanoparticles [22]. Biochemical compounds within the Tulsi extract, particularly flavonoids, play a pivotal role in stabilizing these nanoparticles. Flavonoids act as effective reducing agents, facilitating nanoparticle formation through interactions with various functional groups [51]. As flavonoids convert from their enol to keto forms during this process, hydrogen atoms are released, which in turn reduce Co ions to Co (0) nanoparticles. However, the exact mechanism behind the plant-mediated synthesis of cobalt oxide nanoparticles remains elusive. It is hypothesized that oxygen from the environment or other biochemicals binds to the reduced metal ions, contributing to their stabilization [52]. The electrostatic attraction of metal oxide ions results in the formation of nanoparticles, which are subsequently stabilized by diverse biochemicals present in the plant extract to prevent agglomeration. Despite the need for further detailed mechanistic understanding, the biological synthesis of nanoparticles using plant extracts holds promise due to its non-toxic, cost-effective, and environmentally friendly characteristics.

3.7. Synthesis of SA@Co–Zn–Ce Oxide Nanocomposite

An amount of 0.2 g of Co–Zn–Ce oxide NPs was introduced into a 5% w/w $CaCl_2$ solution and stirred for 60 min. Subsequently, 0.4 g of sodium alginate was added to 50 mL of deionized water. The sodium alginate solution was then added drop by drop to the solution containing the suspension of Co–Zn–Ce oxide nanoparticles and calcium chloride for 1 h with constant stirring. Following the addition of the sodium alginate solution, bead formation could be instantly observed. The resulting solution was subjected to three rounds of washing with deionized water to eliminate any excess unreacted calcium chloride. Finally, the alginate composite was calcined by heating it at 90 °C, and the end product was a powdered nanocomposite, i.e., SA @Co–Zn–Ce, where the nanoparticles were effectively encapsulated within the sodium alginate matrix. The preparation scheme is shown in Figure S12.

The interaction among ternary metal nanoparticles in the SA@Co–Zn–Ce photocatalyst significantly enhances its catalytic efficiency. Co plays a crucial role by facilitating charge transfer and reducing recombination rates through its electron acceptor and donor capabilities. Moreover, its magnetic properties contribute to the photocatalyst's stability and reusability. Zn exhibits a high electron transfer ability, enhancing the oxygen reduction activity and thereby improving the photocatalytic efficiency. It also enhances catalyst stability and reduces corrosion. Ce acts effectively as an oxidizing agent, boosting the generation of reactive oxygen species (ROS) essential for breaking down RR24 dye. Its electronic configuration supports charge transfer and redox reactions. The combined presence of Co and Zn forms a robust Co–Zn double orbital, which enhances electron transfer and catalyst stability. The incorporation of Ce into the system creates a ternary structure that further enhances charge separation and ROS generation. The synergy among Co, Zn, and Ce leads to increased photocatalytic efficiency, improved charge transfer, enhanced stability, and greater reusability, ultimately resulting in the efficient degradation of RR24 dye. Thus, the synergistic effects of Co, Zn, and Ce in the SA@Co–Zn–Ce photocatalyst significantly elevate its photocatalytic performance. This combination leverages the strengths of each metal while compensating for their individual weaknesses, yielding a more efficient photocatalytic material. Enhanced charge transfer, improved stability, and effective pollutant degradation are hallmarks of these advancements.

3.8. Characterization

Several analytical techniques were employed to characterize the synthesized materials, as described below.

3.8.1. Ultraviolet–Visible Spectroscopy

Samples were suspended in water, and their absorbance spectra were recorded in the 200–750 nm range using ultraviolet–visible (UV-Vis) spectroscopy. Measurements using UVD-3400/UVD-3500 (Labomed, Los Angeles, CA, USA) equipment revealed their optical properties. The nanoparticles displayed distinct absorbance peaks in solution, with the bright colors caused by surface plasmon resonance excitation or interband transitions. Cobalt oxide nanoparticles (Co oxide NPs) exhibited a striking dark brown color due to their unique UV-Vis absorption characteristics. Nanoparticles of Co–Zn frequently appeared caramel when coupled with zinc, indicating a change in electronic structure. Co–Zn–Ce oxide nanoparticles changed from caramel to greenish-brown due to cerium's additional absorption properties. By adding sodium alginate as a stabilizing agent to Co–Zn–Ce oxide nanocomposites, the optical properties were further altered, leading to more complex colors such as brownish or grayish-green.

3.8.2. Fourier-Transform Infrared Spectroscopy

FTIR spectroscopy shows interactions between functional groups and metal nanoparticles, especially when multiple functional groups are present in the capping agent. FTIR measurements were conducted using the conventional KBr pellet method using a Perkin Elmer FTIR spectrometer (Perkin Elmer, Waltham, MS, EUA) covering the 4000–400 cm^{-1} spectral range.

3.8.3. X-ray Diffraction

The powder X-ray diffraction (PXRD) analysis of dry nanoparticles and nanocomposites was performed using a Bruker D2-phaser XRD (Bruker, Manama, Bahrain) system equipped with a LYNXEYE XE-T Detector and operated at 220 V/60 Hz. The XRD scan range covered 2θ values from 10 to 80°, with a scan rate of 2° per minute and a step size of 0.05°.

3.8.4. Field-Emission Scanning Electron Microscopy

Field-emission scanning electron microscopy (FE-SEM) was utilized to analyze the surface morphology of nanomaterials and to examine porosity, material uniformity, surface texture, and grain size. FE-SEM was conducted on a JSM IT-100 JEOL (JEOL, Tokyo, Japan).

3.8.5. Zeta Potential

The zeta potential was employed to assess the charge and stability of nanoparticles by quantifying the electric potential difference existing at the interface between a particle surface and the surrounding dispersion medium. The zeta potential was determined using a Malvern Zetasizer Nano ZSP (Malvern Panalytical, Malvern, UK) device. The test was carried out in water with a small amount of KCl (pH 7).

3.9. Dynamic Light Scattering

Dynamic light scattering (DLS) was employed to investigate particle and molecule size distributions as well as dynamic properties in a solution. It was performed in a Litesizer DLS 500 (Anton Paar, Ashland, VA, USA).

3.10. N_2 Adsorption at −196 °C

N_2 adsorption experiments were carried out at −196 °C using a Quanta Instruments NOVA 1200 (Quantachrome, Odelzhausen, Germany). Samples were pretreated at 200 °C for 17 h before the experiments. Brunauer–Emmett–Teller (BET) analysis was utilized to determine the specific surface area, while the Barrett–Joyner–Halenda (BJH) method was employed to analyze the porosity of solid materials.

3.11. Antioxidant Potential

The antioxidant activities of Co oxide NPs, Co–Zn oxide NPs, Co–Zn–Ce oxide NPs, and the sodium alginate composite SA@Co–Zn–Ce were assessed using the 1,1-diphenyl-2-picrylhydrazil (DPPH) radical method [20].

3.12. Photocatalytic Degradation Experiments

The photocatalytic efficacy of the SA@Co–Zn–Ce oxide composite was evaluated by measuring the removal of Reactive Red 24 dye (RR24) in the presence of visible light. Experiments were conducted as follows: a 5 ppm dye concentration and 15 mg of the as-synthesized SA@Co–Zn–Ce oxide composite were used. Before starting the degradation experiment, the mixture of the SA@Co–Zn–Ce oxide nanocomposite and RR24 dye was well sonicated for 10 min in the dark, followed by 60 min of stirring in the dark to establish the adsorption–desorption equilibrium of RR-24. Initially, readings were taken by adsorbing RR24 onto the catalyst in the dark for about 30 min to achieve an equilibrium state (adsorption/desorption) between the dye and the photocatalyst. For the photocatalytic degradation of this reactive dye, the suspension was magnetically stirred for 30 min. To ensure accurate UV/vis measurements throughout the reaction, samples were collected at 10 min intervals and subsequently subjected to centrifugation to eliminate the photocatalyst particles. The efficiency of the SA@Co–Zn–Ce oxide composite in degrading the dye was determined using the following equation:

$$\%\ \text{Degradation efficiency} = (\text{A} - \text{A}_\text{i}/\text{A}) \times 100$$

where A and A_i denote the absorbance of the dye solution before and after photocatalysis, respectively. UV-vis was utilized to observe and assess the degraded RR-24 dye concentrations during the photocatalytic reaction.

The influence of several factors was tested as follows:

3.12.1. Influence of RR24 Dye Concentration

Hydrochloric acid and sodium hydroxide were employed as reagents to study the effect of pH. Various concentrations (5 ppm, 10 ppm, and 15 ppm) of dye were tested to determine the optimal degradation efficiency at specific dye concentrations. For each photoreaction, 20 mg of SA@Co–Zn–Ce oxide catalyst and a 5 ppm RR24 dye solution were added to a pH range between 3 and 7 at a temperature of 30 °C for 100 min to assess the pH factor.

3.12.2. Influence of pH

The effect of temperature on RR24 degradation was tested at pH values of 3.5 and 7. A volume of 50 mL of RR24 dye was degraded using 20 mg of SA@Co–Zn–Ce oxide at the pH values mentioned earlier.

3.12.3. Influence of Temperature

The effect of temperature on RR24 degradation was tested at 20, 30, and 40 °C. A volume of 50 mL of RR24 dye was degraded using 20 mg of SA@Co–Zn–Ce oxide at pH 5.

3.12.4. Effect of Concentration of SA@Co–Zn–Ce Oxide Photocatalyst Dose

Using 10–20 mg of SA@Co–Zn–Ce photocatalyst for 50 mL of dye solution (5 ppm) at pH 5, the effect of photocatalyst dosage on RR24 dye degradation was observed. The duration of each reaction was 100 min.

3.12.5. Influence of H_2O_2 Concentration

To further understand its effects, H_2O_2 was introduced to the photocatalytic reaction at different concentrations ranging from 0 to 10 mmol/L.

3.12.6. Recyclability of SA@Co–Zn–Ce Photocatalyst

In order to test the recyclability of the SA@Co–Zn–Ce oxide photocatalyst, the material was separated through centrifugation at 3000 rpm for 15 min, allowing it to be reused in successive experiments.

3.12.7. Effect of Scavengers

RR24 dye degradation was examined at the ideal pH, temperature, and reaction time using a variety of salts like NaCl, $NaHCO_3$, and Na_2SO_4 [45].

4. Conclusions

In this research, Co oxide NPs, Co–Zn oxide NPs, and Co–Zn–Ce oxide NPs were successfully synthesized through green synthesis by reducing leaf extract from the *Ocimum sanctum* plant. Subsequently, a sodium alginate-anchored Co-Zn-Ce nanocomposite, SA@Co–Zn–Ce oxide NCs, was synthesized by the co-precipitation method. An analysis of the nanoparticles and nanocomposite was conducted using various characterization techniques to elucidate their structural and chemical properties. Among the synthesized nanoparticles, SA@Co–Zn–Ce oxide exhibited the highest antioxidant potential (89%) compared to Co oxide NPs (52%), Co–Zn oxide NPs (81%), and Co–Zn–Ce oxide NPs (88%) nanoparticles, as determined by DPPH radical scavenging activity. This finding underscores the promising applicability of this nanomaterial in combating oxidative stress and related health issues. Furthermore, SA@Co–Zn–Ce oxide NPs demonstrated remarkable photocatalytic potential in the degradation of Reactive Red 24 dye and could be reused up to four cycles. Kinetic studies confirmed that the photodegradation using this catalyst followed a pseudo-first-order reaction, highlighting the efficiency of the developed nanocomposite for environmental remediation applications. This research not only contributes to the bioengineering and analysis of novel nanomaterials but also demonstrates the potential of SA@Co–Zn–Ce oxide NCs as highly effective catalysts in the remediation of organic pollutants, offering promising prospects for addressing environmental pollution challenges.

Supplementary Materials: The following supporting information can be downloaded at https://www.mdpi.com/article/10.3390/catal14080471/s1, Figure S1. UV-vis absorption for *Ocimum sanctum* leaf extract; Figure S2. Particle size distribution (PSD) of SA@Co-Zn-Ce nanocomposite; Figure S3. λ max of RR24; Figure S4. Factors affecting photocatalytic degradation of RR24; Figure S5. Degradation kinetics for RR24 dye by varying catalyst dose: Ao/At vs time (a) and ln (At/Ao) versus time (b); Figure S6. Degradation kinetics for RR24 dye by varying RR24 dye concentration: Ao/At vs time (a) and ln (At/Ao) versus time (b); Figure S7. Degradation kinetics for RR24 dye by varying pH: Ao/At vs time (a) and ln (At/Ao) versus time (b); Figure S8. Schematic representation for preparation of leaf extract of *Ocimum sanctum*; Figure S9. Biosynthesis of cobalt NPs by *Ocimum sanctum*; Figure S10. Biosynthesis of Co-Zn NPs by *Ocimum sanctum*; Figure S11. Biosynthesis of Co-Zn-Ce NPs by *Ocimum sanctum*; Figure S12. Synthesis of SA@Co-Zn-Ce NCs; Table S1. % DPPH Free Radical Scavenging potential; Table S2. Summary of R^2 and rate constant k_{obs} (min^{-1}) for photocatalytic degradation of RR24 dye using SA@Co-Zn-Ce nanocomposite.

Author Contributions: S.F.: writing—original draft preparation, investigation, methodology; S.J.: writing—original draft preparation, investigation; H.A.: data curation, formal analysis; A.A.: formal analysis; D.F.B.: formal analysis; O.M.A.: formal analysis, resources; S.A.C.C.: supervision, visualization; writing—review and editing; M.B.T.: project administration, supervision. All authors have read and agreed to the published version of the manuscript.

Funding: This research was funded by Taif University, Saudi Arabia, project number (TU-DSPP-2024-276).

Data Availability Statement: All data are present within the manuscript body.

Acknowledgments: M.B.T acknowledges support from the HEC (Higher Education Commission) of Pakistan. S.A.C.C. acknowledges Fundação para a Ciência e Tecnologia and Ministério da Ciência, Tecnologia e Ensino Superior through project DOIs: 10.54499/LA/P/0008/2020, 10.54499/UIDP/50006/2020, 10.54499/UIDB/50006/2020, and Scientific Employment Stimulus—Institutional Call (DOI 10.54499/CEECINST/00102/2018/CP1567/CT0026).

Conflicts of Interest: The authors declare no conflicts of interest.

References

1. Datta, K.; Chakraborty, S.; Roychoudhury, A. Management of Soil, Waste and Water in the Context of Global Climate Change. In *Environmental Nexus for Resource Management*; CRC Press: Boca Raton, FL, USA, 2025; pp. 1–26.
2. Babaniyi, B.R.; Ogundele, O.D.; Bisi-Omotosho, A.; Babaniyi, E.E.; Aransiola, S.A. Remediation approaches in environmental sustainability. In *Microbiology for Cleaner Production and Environmental Sustainability*; CRC Press: Boca Raton, FL, USA, 2023; pp. 321–346.
3. dos Santos, J.C.V.; de Santana Costa, A.F.; de Lima e Silva, T.A.; Sarubbo, L.A.; de Luna, J.M. New Trends in the Textile Industry: Utilization and Application of Biosurfactants. In *Advancements in Biosurfactants Research*; Springer: Berlin/Heidelberg, Germany, 2023; pp. 215–223.
4. Palanivelan, R.; Ramya, S.; Aradhana, S.; Ayyasamy, P.; Sabour, A.A.A.; Muthusamy, R.; Narayanan, M. Bioprospective decolourization of reactive azo dyes at pilot scale by a developed bacterial consortium using the RSM and CCD model. *Biomass Convers. Biorefinery* **2024**, 1–18. [CrossRef]

5. Nandana, E.; Dwivedi, A.H.; Nidheesh, P. Role of biochar in superoxide-dominated dye degradation in catalyst-activated peroxymonosulphate process. *Chemosphere* **2024**, *356*, 141945. [CrossRef] [PubMed]
6. Wen, L.; Wang, D.; Xi, J.; Tian, F.; Liu, P.; Bai, Z.-W. Heterometal modified Fe3O4 hollow nanospheres as efficient catalysts for organic transformations. *J. Catal.* **2022**, *413*, 779–785. [CrossRef]
7. Crozier, V. *The Brave New Worlds of Green Science Fiction: Ecocritical Discourse in the Three-Body Problem and the Long Earth Series*; Liverpool John Moores University: Liverpool, UK, 2023.
8. Guo, S.; Chen, M.; Wei, Y.; You, L.; Cai, C.; Wei, Q.; Zhou, K. Designing hierarchically porous zero-valent iron via 3D printing to degrade organic pollutants by activating peroxymonosulfate using high-valent iron-oxo species. *Chem. Eng. J.* **2023**, *476*, 146523. [CrossRef]
9. Vaiano, V.; De Marco, I. Removal of azo dyes from wastewater through heterogeneous photocatalysis and supercritical water oxidation. *Separations* **2023**, *10*, 230. [CrossRef]
10. Bibi, A.; Bibi, S.; Abu-Dieyeh, M.; Al-Ghouti, M.A. Towards sustainable physiochemical and biological techniques for the remediation of phenol from wastewater: A review on current applications and removal mechanisms. *J. Clean. Prod.* **2023**, *417*, 137810. [CrossRef]
11. Amir, M.; Vohra, M.; Raj, R.G.; Osoro, I.; Sharma, A. Adaptogenic herbs: A natural way to improve athletic performance. *Health Sci. Rev.* **2023**, *7*, 100092. [CrossRef]
12. Islam, T.; Rahaman, M.M.; Mia, M.N.; Ara, I.; Islam, M.T.; Alam Riaz, T.; Araújo, A.C.; de Lima Silva, J.M.F.; de Lacerda, B.C.G.V.; de Andrade, E.M. Therapeutic Perspectives of Metal Nanoformulations. *Drugs Drug Candidates* **2023**, *2*, 232–278. [CrossRef]
13. Ali, S.S.; Abdelkarim, E.A.; Elsamahy, T.; Al-Tohamy, R.; Li, F.; Kornaros, M.; Zuorro, A.; Zhu, D.; Sun, J. Bioplastic production in terms of life cycle assessment: A state-of-the-art review. *Environ. Sci. Ecotechnology* **2023**, *15*, 100254. [CrossRef]
14. Wang, H.; Liu, X.; Wang, Y.; Tian, Y.; Huang, Y.; Huang, D.; Liu, X. Carbon nanotubes as a nanocatalyst and nanoreactor for the efficient treatment of pharmaceutical wastewater via $CaSO_3$ activation. *Environ. Sci. Nano* **2024**, *11*, 1978–1984. [CrossRef]
15. Butt, F.S.; Safdar, M.; Lewis, A.; Mazlan, N.A.; Radacsi, N.; Fan, X.; Arellano-García, H.; Huang, Y. Superhydrophobic ZIF-67 with exceptional hydrostability. *Mater. Today Adv.* **2023**, *20*, 100448. [CrossRef]
16. Samriti; Shukla, K.; Gupta, R.; Gupta, R.K.; Prakash, J. Highly efficient visible light active doped metal oxide photocatalyst and SERS substrate for water treatment. *Environ. Sci. Pollut. Res.* **2023**, *30*, 34054–34068. [CrossRef] [PubMed]
17. Ramakrishnan, R.; Kim, J.T.; Roy, S.; Jayakumar, A. Recent advances in carboxymethyl cellulose-based active and intelligent packaging materials: A comprehensive review. *Int. J. Biol. Macromol.* **2024**, *259*, 129194. [CrossRef] [PubMed]
18. Anwer, A.H.; Ahtesham, A.; Shoeb, M.; Mashkoor, F.; Ansari, M.Z.; Zhu, S.; Jeong, C. State-of-the-art advances in nanocomposite and bio-nanocomposite polymeric materials: A comprehensive review. *Adv. Colloid. Interface Sci.* **2023**, *318*, 102955. [CrossRef] [PubMed]
19. Joseph, T.M.; Al-Hazmi, H.E.; Śniatała, B.; Esmaeili, A.; Habibzadeh, S. Nanoparticles and nanofiltration for wastewater treatment: From polluted to fresh water. *Environ. Res.* **2023**, *238*, 117114. [CrossRef] [PubMed]
20. Li, L.; Fu, R.; Zou, J.; Wang, S.; Ding, J.; Han, J.; Zhao, M. Research progress of iron-based catalysts in ozonation wastewater treatment. *ACS EST Water* **2023**, *3*, 908–922. [CrossRef]
21. Zaharia, C.; Suteu, D. Empirical Modeling by Active Central Composite Rotatable Design: Orange 16 Dye Biosorption onto Biosorbents Based on Residual Bacterial *Lactobacillus* sp. Biomass. *Separations* **2023**, *10*, 279. [CrossRef]
22. Wang, J.; She, W.; Li, X.; Li, J.; Li, Z.; Mao, G.; Li, W.; Li, G. Efficient tandem catalytic N-alkylation of nitroarenes with alcohols via a Co/CeO_2-CN catalyst derived from a tri-metallic Co-Zn-Ce coordination polymer. *Appl. Surf. Sci.* **2022**, *592*, 153250. [CrossRef]
23. Luo, H.; Sun, Y.; Zhang, L. Effects of macroprudential policies on ecological footprint: The moderating role of environmental policy stringency in the top 11 largest countries. *Sci. Rep.* **2024**, *14*, 7423. [CrossRef] [PubMed]
24. Alelwani, W.; Bibi, I.; Sharif, M.; Saleem, M.; Rizwan, M. The Biogenic Synthesis of Bimetallic Ag/ZnO Nanoparticles: A Multifunctional Approach for Methyl Violet Photocatalytic Degradation and the Assessment of Antibacterial, Antioxidant, and Cytotoxicity Properties. *Nanomaterials* **2023**, *13*, 2079. [CrossRef]
25. Logeswari, V.; Yamini, S.; Pavithra, P.; Papitha, A.; Lakshmi, D. Study of Antioxidant, Antimicrobial and Cytotoxic Activities of Ag-Co Bimetallic Nanoparticles Biosynthesized from Red Alga (*Amphiroa* sp.). *Indian J. Sci. Technol.* **2024**, *17*, 2013–2023. [CrossRef]
26. Faisal, S.; Jan, F.A.; Saleem, S.; Ullah, R.; Wajidullah; Ullah, N.; Salman. *Juglans regia* L. mediated synthesis of cobalt oxide and zinc-doped cobalt oxide nanoparticles: Characterization and evaluation for environmental, antibacterial and cytotoxic potential. *Nanotechnol. Environ. Eng.* **2022**, *7*, 675–689. [CrossRef]
27. Ansari, A.A.; Alam, M. Electrochemical sensitive detection of hydrazine through cobalt-doped cerium oxide nanostructured platform. *J. Mater. Sci. Mater. Electron.* **2021**, *32*, 13897–13905. [CrossRef]
28. Daniel, S.; Kumar, R.; Sathish, V.; Sivakumar, M.; Sunitha, S.; Sironmani, T.A. Green synthesis (*Ocimum tenuiflorum*) of silver nanoparticles and toxicity studies in zebra fish (*Danio rerio*) model. *Int. J. NanoSci Nanotechnol.* **2011**, *2*, 103–117.
29. Hafeez, M.; Shaheen, R.; Akram, B.; Haq, S.; Mahsud, S.; Ali, S.; Khan, R.T. Green synthesis of cobalt oxide nanoparticles for potential biological applications. *Mater. Res. Express* **2020**, *7*, 025019. [CrossRef]
30. Al-Fakeh, M.S. Synthesis, thermal stability and kinetic studies of copper (II) and cobalt (II) complexes derived from 4-aminobenzohydrazide and 2-mercaptobenzothiazole. *Eur. Chem. Bull.* **2020**, *9*, 403–409. [CrossRef]

31. Manojkumar, K.; Prasad, B.; Kranthi, Y.; Varma, J.; Vinay, K.; Amaranatha Reddy, D.; Subramanyam, K. Benchmark analysis on magnetic and photoluminescence properties of selective metal ions doped ZnS nanoparticles. *J. Supercond. Nov. Magn.* **2019**, *32*, 2489–2500. [CrossRef]
32. Aprilliza, M. Characterization and properties of sodium alginate from brown algae used as an ecofriendly superabsorbent. In Proceedings of the IOP Conference Series: Materials Science and Engineering, Bali, Indonesia, 26–27 July 2016; p. 012019.
33. Moulder, J.F.; Stickle, W.F.; Sobol, P.E.; Bomben, K.D. *Handbook of X-ray Photoelectron Spectroscopy*; Perkin-Elmer Corporation: Eden Prairie, MN, USA, 1992.
34. Riđošić, M.; Nikolić, N.D.; Salicio-Paz, A.; García-Lecina, E.; Živković, L.S.; Bajat, J.B. Zn-Co-CeO_2 vs. Zn-Co Coatings: Effect of CeO_2 Sol in the Enhancement of the Corrosion Performance of Electrodeposited Composite Coatings. *Metals* **2021**, *11*, 704. [CrossRef]
35. Jia, Z.; Li, J.; Gao, L.; Yang, D.; Kanaev, A. Dynamic light scattering: A powerful tool for in situ nanoparticle sizing. *Colloids Interfaces* **2023**, *7*, 15. [CrossRef]
36. Walton, K.S.; Snurr, R.Q. Applicability of the BET method for determining surface areas of microporous metal− organic frameworks. *J. Am. Chem. Soc.* **2007**, *129*, 8552–8556. [CrossRef]
37. Ullah, S.; Bustam, M.A.; Assiri, M.A.; Al-Sehemi, A.G.; Sagir, M.; Kareem, F.A.A.; Elkhalifah, A.E.; Mukhtar, A.; Gonfa, G. Synthesis, and characterization of metal-organic frameworks-177 for static and dynamic adsorption behavior of CO_2 and CH_4. *Microporous Mesoporous Mater.* **2019**, *288*, 109569. [CrossRef]
38. Barzinjy, A.A.; Azeez, H.H.J.S.A.S. Green synthesis and characterization of zinc oxide nanoparticles using Eucalyptus globulus Labill. leaf extract and zinc nitrate hexahydrate salt. *SN Appl. Sci.* **2020**, *2*, 991. [CrossRef]
39. Guo, G.; Zhu, X.; Shi, F.; Wang, A.; Wang, W.; Mu, J.; Wan, Q.; Zhang, R. Photocatalytic degradation of CI Reactive Red 24 solution with K6SiW11O39SnII. *J. Environ. Sci.* **2013**, *25*, S80–S84. [CrossRef]
40. Van, H.T.; Nguyen, L.H.; Dang, N.; Chao, H.-P.; Nguyen, Q.T.; Nguyen, T.H.; Nguyen, T.B.L.; Van Thanh, D.; Nguyen, H.D.; Thang, P.Q. The enhancement of reactive red 24 adsorption from aqueous solution using agricultural waste-derived biochar modified with ZnO nanoparticles. *RSC Adv.* **2021**, *11*, 5801–5814. [CrossRef] [PubMed]
41. Agustina, T.; Wijaya, Y.; Mermaliandi, F. Degradation of reactive red 2 by Fenton and photo-Fenton oxidation processes. *ARPN J. Eng. Appl. Sci.* **2016**, *11*, 5227–5231.
42. Zhang, Y.; Li, M.; Zhang, Q.; Li, Z.; Zhong, M.; Li, J.; Abodif, A.M. Iron phthalocyanine doped carbon-based as a bifunctional material for peroxymonosulfate activation toward Reactive Red 24 degradation: Consolidated adsorption and multiple oxidation. *J. Water Process Eng.* **2023**, *51*, 103476. [CrossRef]
43. Mondol, B.; Sarker, A.; Shareque, A.; Dey, S.C.; Islam, M.T.; Das, A.K.; Shamsuddin, S.M.; Molla, M.A.I.; Sarker, M. Preparation of activated carbon/TiO_2 nanohybrids for photodegradation of reactive red-35 dye using sunlight. *Photochem.* **2021**, *1*, 54–66. [CrossRef]
44. Li, M.; Li, J.-T.; Sun, H.-W. Decolorizing of azo dye Reactive red 24 aqueous solution using exfoliated graphite and H_2O_2 under ultrasound irradiation. *Ultrason. Sonochemistry* **2008**, *15*, 717–723. [CrossRef]
45. Duan, L.; Wang, B.; Heck, K.N.; Clark, C.A.; Wei, J.; Wang, M.; Metz, J.; Wu, G.; Tsai, A.-L.; Guo, S. Titanium oxide improves boron nitride photocatalytic degradation of perfluorooctanoic acid. *Chem. Eng. J.* **2022**, *448*, 137735. [CrossRef]
46. Chen, K.; Ku, Y.; Lee, K. The study of ultrasonic irradiation on decomposition of 2-chlorophenol in aqueous solution. In Proceedings of the 19th Wastewater Treatment Technology Conference, Taiwan, 27–28 November 1994; p. 14.
47. Neppolian, B.; Park, J.-S.; Choi, H. Effect of Fenton-like oxidation on enhanced oxidative degradation of para-chlorobenzoic acid by ultrasonic irradiation. *Ultrason. Sonochemistry* **2004**, *11*, 273–279. [CrossRef]
48. Zhang, L.; Chen, L.; Liu, X.; Zhang, W. Effective removal of azo-dye orange II from aqueous solution by zirconium-based chitosan microcomposite adsorbent. *RSC Adv.* **2015**, *5*, 93840–93849. [CrossRef]
49. Hung, H.-M.; Ling, F.H.; Hoffmann, M.R. Kinetics and mechanism of the enhanced reductive degradation of nitrobenzene by elemental iron in the presence of ultrasound. *Environ. Sci. Technol.* **2000**, *34*, 1758–1763. [CrossRef]
50. Blanchard, G.; Maunaye, M.; Martin, G. Removal of heavy metals from waters by means of natural zeolites. *Water Res.* **1984**, *18*, 1501–1507. [CrossRef]
51. Jakab, M.; Presuel-Moreno, F.; Scully, J. Effect of molybdate, cerium, and cobalt ions on the oxygen reduction reaction on AA2024-T3 and selected intermetallics: Experimental and modeling studies. *J. Electrochem. Soc.* **2006**, *153*, B244. [CrossRef]
52. Gilani, Z.A.; Khalid, M.; Hussain, G.; Shar, M.A.; Ali, S.M.; Khan, M.A.; Sheikh, F.A.; Alhazaa, A. Impact of cerium substitution cobalt–zinc spinel ferrites for the applications of high frequency devices. *Phys. B Condens. Matter* **2023**, *660*, 414873.

Disclaimer/Publisher's Note: The statements, opinions and data contained in all publications are solely those of the individual author(s) and contributor(s) and not of MDPI and/or the editor(s). MDPI and/or the editor(s) disclaim responsibility for any injury to people or property resulting from any ideas, methods, instructions or products referred to in the content.